Post-Print

This is the accepted version of:

When citing this work, cite the original published paper.

Perpendicular Blade-Vortex-Interaction over an Oscillating Airfoil in Light Dynamic Stall

G. Droandi[1], G. Gibertini[2], A. Zanotti[1,*]

Politecnico di Milano, Dipartimento di Scienze e Tecnologie Aerospaziali
Campus Bovisa, Via La Masa 34, 20156 Milano, Italy

Abstract

An experimental and numerical study was performed to investigate the effects of perpendicular blade vortex interactions on the aerodynamic performance of an oscillating airfoil. The selected test cases studied the aerodynamic interaction of a stream-wise vortex impacting on a NACA 23012 airfoil oscillating in light dynamic stall regime, representing a typical condition of the retreating blade of a helicopter in forward flight. The analysis of particle image velocimetry surveys and time-accurate simulations results enabled to point out the different effects due to the blade pitching motion on the interacting flow field. Thus, numerical results enabled to achieve a detailed insight about the aerodynamic loads acting on the oscillating airfoil in the interacting cases. In particular, the comparison with the clean airfoil case shows that a severe loss of performance is produced by the interaction of the vortex during the airfoil downstroke motion, as the vortex impact triggers the local stall of the blade section.

Keywords: Blade-vortex-interaction, Oscillating airfoil, Computational fluid dynamics, Particle Image Velocimetry.

1. Introduction

The aerodynamic interactions between helicopter rotor blades and its own tip vortices represent an important topic of investigation in rotorcraft research field due to the adverse influence produced on rotor noise (Schmitz and Yu, 1983; Yu, 2000) and rotor performance. In fact, due to these interactions the resulting pressure fluctuations on the blade surface produce highly unsteady aerodynamic loads. Moreover, blade-vortex interactions (BVIs), occurring mainly when the helicopter is slightly descending (Shockey et al., 1997) and the tip vortex wake remains in the region of the rotor disk, are an important source of vibrations and instability. Literature distinguishes different classes of BVIs depending on the direction of the impacting

---

*Corresponding author
Email address:* `alex.zanotti@polimi.it` (A. Zanotti)
[1]Postdoctoral Fellow
[2]Assistant Professor

vortex axis with respect to the blade span. In particular, parallel BVI occurs when the vortex and the blade axes are nominally parallel, perpendicular BVI when the axes are perpendicular and in parallel planes, orthogonal BVI when the axes are in orthogonal planes and finally oblique BVI when oblique collisions occur between the vortex and the blade. An extensive review on these interactions is given in Rockwell (1998) and Conlisk (2001).

An important effort was made in both experimental and numerical research fields to provide a better understanding of the physics involved in these aerodynamic interactions and their effects on rotor performance and handling qualities. In particular, in the past years different suitable computational models were developed to reproduce BVI in numerical simulations of rotor flow field. Among these studies, Rahier and Delrieux (1999) developed different vortex models with the capability to deform during close interactions. The suitability of these models to obtain a proper evaluation of noise and loads was verified by comparison with experimental data. More recently, Zioutis et al. (2004) investigated the influences of numerical simulation of different BVI cases on the computational results of rotor blade downwash distribution and aerodynamic loading. A high-fidelity, implicit large-eddy simulation was used by Garmann and Visbal (2015) to investigate the unsteady interactions resulting from a stream-wise vortex impinging upon a finite plate at different span-wise positions.

A complete analysis including numerical modeling and wind tunnel data for the evaluation of the effects of BVIs on rotor noise was given in Glegg et al. (1999) and Yu (2000), showing that, due to its low unsteadiness, the noise effects of perpendicular BVI are less significant with respect to parallel BVI. Indeed, the sudden pressure fluctuations induced by travelling vortices in parallel BVI result in the propagation of strong impulsive (harmonic) noise, while subsequent perpendicular BVIs produce a continuous (broadband) noise characterised by a much lower intensity compared to the harmonic noise. Nevertheless, the locally-induced angles of incidence produced by perpendicular interactions can trigger dynamic stall in the retreating blade and produce rotor vibrations.

Among the experimental activities, Wittmer and Devenport (1999a,b) investigated the turbulent flow field produced by a perpendicular interaction of a stream-wise vortex with a still blade section model, showing that the extent of the turbulent flow region and the turbulent intensity increase due to the interaction of the vortex with the blade section wake. In the past years the use of particle image velocimetry (PIV) provided quantified visualizations of the flow generated during BVIs (Horner et al., 1996; Green et al., 2000). Thanks to the development of stereoscopic PIV set up, a more detailed insight into the three-dimensional nature of the interacting flow field was gained, as done by Green et al. (2006) for the investigation of orthogonal BVI.

The present work describes an experimental and numerical study carried out at Politecnico di Milano about the investigation of the interaction of a stream-wise vortex over a NACA 23012 airfoil oscillating in light dynamic stall regime (McCroskey, 1981; Leishman, 2000).

Although, as already mentioned, the BVI phenomenon is very important in the rotorcraft research field,

the aim of the present study was not the reproduction of a real helicopter blade condition but a basic investigation of the pure perpendicular vortex-airfoil interaction. In addition to other similar studies, the present work includes the investigation of the effect of airfoil oscillation. Indeed, past experimental activities (see, for example, (Wittmer and Devenport, 1999a,b; Ham, 1975; Rife and Devenport, 1992)) tipically used a set up where a still blade section model is struck by a perpendicular vortex without taking into account the oscillation of the target model. However, the contribution of the target airfoil oscillation produces important effects on the interacting flow behaviour, as shown in the previous work by Zanotti et al. (2014a), where the results of PIV surveys carried out with the target model at the same angle of attack in steady and oscillating conditions are compared.

A problem influencing the stream-wise vortices generated inside a wind-tunnel test chamber is the low-frequency oscillation of the vortex centre-line, called *vortex wandering* (Devenport et al., 1996; Iungo et al., 2009), that apparently does not affect free-stream vortices. Due to this wandering, the average vortex is more diffused compared to the actual instantaneous one. For the present set up, the wandering of the isolated vortex was analysed in a previous experimental work (Gibertini et al., 2014) by a statistical analysis showing that the wandering amplitude of the investigated stream-wise vortex is relatively small, with a standard deviation sensibly less than 20% of the vortex core in the span-wise and vertical directions.

The main focus of the present study is the analysis of the effects of the stream-wise vortex interactions on the blade aerodynamic performance. Due to the high unsteadiness and three-dimensionality of the interacting flow field the measurement of the aerodynamic loads acting on the whole oscillating airfoil span represents a very demanding and challenging task. Thus, time-accurate CFD simulations reproducing the experiments were carried out to evaluate the airloads distribution acting on the target airfoil during the complete oscillation cycle. The blade performance variation due to the vortex interaction was analysed by comparison with the results of CFD simulations performed also for the clean oscillating airfoil. The reliability of the CFD simulations was checked by comparison with the results of stereo PIV surveys carried out over the upper surface of the oscillating airfoil. Moreover, CFD results were also suitable to achieve a more complete analysis of the overall interacting flow field behaviour along blade span over the whole oscillation cycle.

The structure of the article is the following. In section 2, the experimental set up is outlined. In section 3, the CFD solver and the numerical model used in the present activity are described. Section 4 reports the comparison of the experimental and numerical flow fields as well as the aerodynamic performance analysis for the oscillating airfoil with perpendicular BVI obtained from the CFD simulations results. Final considerations and comments are given in section 5.

Nomenclature

α	Angle of attack [deg]
α_m	Mean angle of attack [deg]
α_a	Pitching oscillation amplitude [deg]
ρ	Air density [kg/m^3]
ω	Circular frequency [rad/s]
$\boldsymbol{\Omega}$	Vorticity tensor
$\|\Omega\|$	Vorticity magnitude [1/s]
Ω_x	Stream-wise vorticity component [1/s]
Ω_y	Span-wise vorticity component [1/s]
b	Oscillating airfoil model span [m]
BVI	Blade Vortex Interaction
c	Blade section model chord [m]
CFD	Computational Fluid Dynamics
C_{D^w}	Drag coefficient $= D/\frac{1}{2}\rho U_\infty^2 cb$
C_L	Sectional lift coefficient $= L/\frac{1}{2}\rho U_\infty^2 c$
C_{L^w}	Lift coefficient $= L/\frac{1}{2}\rho U_\infty^2 cb$
C_M	Sectional pitching moment coefficient about the airfoil quarter chord $M/\frac{1}{2}\rho U_\infty^2 c^2$
C_{M^w}	Pitching moment coefficient about the airfoil quarter chord $M/\frac{1}{2}\rho U_\infty^2 c^2 b$
C_p	Pressure coefficient $(p - p_\infty)/\frac{1}{2}\rho U_\infty^2$
d	Distance along the normal to chord direction [m]
D	Drag [N]
$\Delta\xi$	Minimum stream-wise grid spacing on the oscillating airfoil surface
$\Delta\zeta$	Minimum span-wise grid spacing on the oscillating airfoil surface
ΔX	Minimum grid spacing in X direction for the vortex grid
ΔY	Minimum grid spacing in Y direction for the vortex grid
ΔZ	Minimum grid spacing in Z direction for the vortex grid
DAER	Dipartimento di Scienze e Tecnologie Aerospaziali
DSV	Dynamic Stall vortex
f	Oscillation frequency [Hz]
k	Reduced frequency $= \pi f c / U_\infty$
L	Lift [N]
LE	Leading edge
M	Pitching moment coefficient about the airfoil quarter chord [Nm]
M_a	Mach number

N_{Tot}	Total number of grid elements
N_ξ	Number of grid elements along the oscillating airfoil section
N_ζ	Number of grid elements along the oscillating airfoil span
N_η	Number of layers in the oscillating airfoil boundary layer
N_X	Number of grid elements in X direction for the vortex grid
N_Y	Number of grid elements in Y direction for the vortex grid
N_Z	Number of grid elements in Z direction for the vortex grid
OG	Oscillating airfoil grid
p	Pressure [Pa]
p_∞	Free-stream pressure [Pa]
PIV	Particle Image Velocimetry
Q	Q criterion $= 1/2(\|\mathbf{\Omega}\|^2 - \|\mathbf{S}\|^2)$ [$1/s^2$]
R_e	Reynolds number
ROSITA	ROtorcraft Software ITAly
$\mathbf{S}$	Strain–rate tensor
TE	Trailing edge
TS	Time steps
u	Chord-wise velocity [m/s]
v	Span-wise velocity component [m/s]
w	Vertical velocity component [m/s]
$|U|$	Velocity magnitude [m/s]
U_∞	Free-stream velocity [m/s]
VG	Vortex generator airfoil grid
x	Stream-wise coordinate axis
X	Chord-wise coordinate axis
Y	Span-wise coordinate axis
Z	Vertical coordinate axis

2. Experimental Set up

The experimental activity on perpendicular BVI was carried out at the Aerodynamics Laboratory of the Dipartimento di Scienze e Tecnologie Aerospaziali (DAER) of Politecnico di Milano. The wind tunnel had a $1\ m \times 1.5\ m$ test section with a maximum free-stream velocity of $55\ m/s$, and a free-stream turbulence level less than 0.1 %.

2.1. BVI Test rig set up

The experimental set up consists of two airfoil models both with constant NACA 23012 section (Leishman, 1990) and a 0.3 m chord length. The upstream model, used as vortex generator, spanned about half the test section width and was clamped at $\alpha = 10°$. The vortex generator model is attached to a vertical traversing system to adjust the required position of the stream-wise vortex for the selected test condition. The second airfoil model with an aspect ratio of 3.1 represented the target of the impacting vortex and was pivoted around the axis at 25 % of the airfoil chord by means of a brushless servomotor equipped with a 12:1 gear drive. An absolute digital encoder with 2048 imp/rev was directly mounted on the pitching model to be used for feedback control of the pitching motion and to provide the trigger signal for the acquisition of the PIV images at the selected angle of attack of the target model. The airfoil models were positioned inside the wind tunnel test section so that the leading edge of the oscillating model was 3.5 c past the trailing edge of the vortex generator model. This distance was chosen to maximise the distance between the two airfoils taking into account the test section length. In fact, in order to obtain an isolated vortex from the fore airfoil, the vortex sheet issued from the trailing edge must have enough space to be well enrolled and concentrated in the stream-wise vortex. Further details on the pitching airfoil experimental rig can be found in Zanotti et al. (2011); Zanotti and Gibertini (2013). A schematic layout of the experimental rig including the stereo PIV set up is shown in Fig. 1.
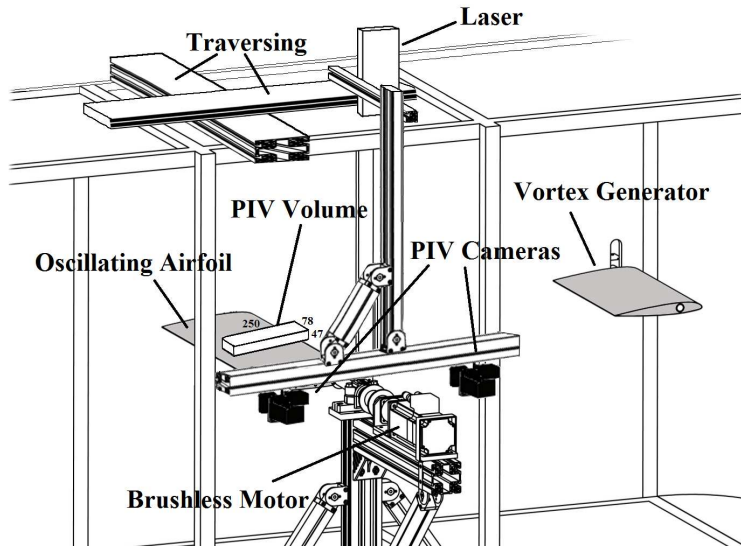

Figure 1: Layout of the perpendicular BVI test rig including the stereo PIV measurement volume (dimensions in mm).

2.2. Stereo PIV set up

The stereo PIV survey were carried out over longitudinal X-Z plane windows at different span-wise locations of the oscillating airfoil upper surface. The dimensions of the measurement window was 250 $mm \times$

47 mm with its lower side at 26 mm from the target airfoil leading edge (see the sketch in Fig. 2). The spacing between the measurement planes in the span-wise direction was 3 mm, which is comparable to the dimensions of the interrogation window used for the correlation of the image pairs. Thus, this technique enabled to reconstruct the three-dimensional flow field over a volume centered on the midspan section of the oscillating airfoil with 78 mm width (see the sketch in Fig. 1). In order to achieve a higher resolution of the image pairs, the measurement area was composed of two windows with a small overlapping band between them. The PIV system comprised a Litron NANO-L-200-15 Nd:Yag double pulsed laser with a 200 mJ output energy and a wavelength of 532 nm that was positioned on the top of the wind tunnel test section. Two Imperx ICL-B1921M CCD cameras with a 12 bit, 1952×1112 pixel array equipped with a Nikkor 50 mm lens and tilting type lens for correct focusing of the measurement window were employed for the image pairs acquisition. The tilting lens mountings were adjusted in order to achieve the Scheimpflug condition. The laser and the cameras were connected by a metallic arm and mounted to a double axis traversing system in order to simultaneously move the laser sheet and the measurement window along the oscillating model span-wise and chord-wise directions. The two laser pulses were synchronized with the image pair exposure by a 6-channel Quantum Composer QC9618 pulse generator. Indeed, the digital encoder signal triggered the laser and the cameras with the angle of attack of the oscillating model selected for the survey every 1/rev. The digital images acquisition was performed using a GigaEthernet EBus connection. The seeding of the wind tunnel test section was carried out by a particle generator with Laskin atomizer nozzles supplying small oil droplets with a diameter in the range of 1-2 μm. Furter details about the PIV experimental set up can be found in Zanotti et al. (2014a). The image pair analysis was carried out by the PIVview 3C software (PIVTEC, 2010). In particular, the multigrid interrogation method (Raffel et al., 1998) was used starting from a 96 pixels × 96 pixel to a 32 pixel × 32 pixel interrogation window. The accuracy of the stereo PIV measurements was estimated to lead to a maximum displacement error of 0.1 px corresponding to less than 3 % of the free-stream velocity (Zanotti et al., 2014a; De Gregorio et al., 2012).

A total number of 100 image pairs were acquired for each measurement plane. This choice was considered a fair compromise between the need to obtain reliable phase-averages of the three-dimensional velocity fields and an admissible run time considering the high number of the span-wise measurement planes performed during the experiments. However, a statistical convergence study was performed to prove the suitability of the present procedure to obtain an accurate description of the behaviour of the investigated unsteady flow field. This study was accomplished performing a phase-average over half the number of the acquired image pairs. The results compared with the ones based on the full data base show very small differences on the three velocity components. In particular, for the test condition characterised by a quite regular flow behaviour a maximum discrepancy lower than 1% of the free-stream velocity was found. For the test condition characterised by massive flow separation, an average difference on the order of 2% of the free-stream velocity was found with a maximum discrepancy up to an order of 10% of the free-stream velocity

only in few data points (less than 1% of the total data set). Thus, the statistical convergence was proven by evaluating the phase-averaged flow fields over 75 image pairs, which leads to an halving of the maximum differences.
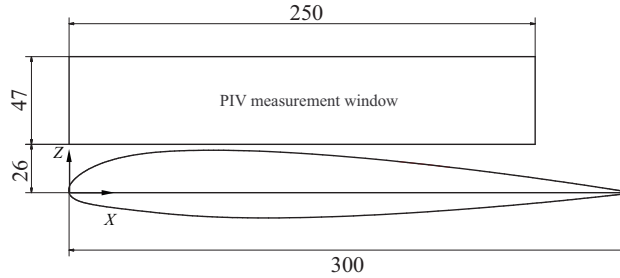

Figure 2: Sketch of the stereo PIV measurement area on the oscillating airfoil upper surface (dimensions in mm).

3. Numerical Simulations

The perpendicular BVI was numerically investigated using the CFD solver ROSITA (Biava, 2007; Biava et al., 2003) developed at DAER. The numerical model, built to reproduce the experimental test rig geometry, represented both the oscillating NACA 23012 airfoil and the upstream vortex generator airfoil inside the wind tunnel section. A top view of the geometry reproduced in the calculations is shown in Fig. 3 where also the Cartesian reference system is reported. The origin of the reference system was located on the leading edge of the oscillating airfoil with the Z axis pointing upward.
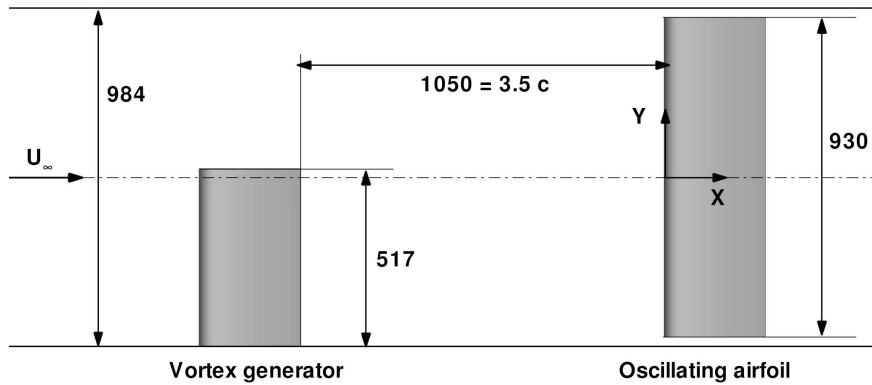

Figure 3: Scheme of the models set up inside the wind tunnel test section (top view) (dimensions in mm).

3.1. Flow solver ROSITA

The flow solver ROSITA numerically integrates the unsteady compressible Reynolds Averaged Navier-Stokes (RANS) equations, coupled with the one-equation turbulence model by Spalart and Allmaras (1992).

8

Multiple moving multi-block grids can be employed to build an overset grid system using the Chimera technique. To allow the solution of the flow field in overset grid systems, the Navier-Stokes equations are formulated in terms of the absolute velocity, expressed in a relative frame of reference linked to each component grid. The equations are discretised in space by means of a cell-centred finite-volume implementation of the Roe's scheme (Roe, 1981). Second order accuracy is obtained through the use of MUSCL extrapolation supplemented with a modified version of the Van Albada limiter, as suggested by Venkatakrishnan (Venkatakrishnan, 1993). The Gauss theorem and a cell-centred discretisation scheme are used to compute the viscous terms of the equations. Time advancement is carried out with a dual-time formulation (Jameson, 1991), employing a 2nd order backward differentiation formula to approximate the time derivative and a fully unfactored implicit scheme in pseudo-time. The equation for the state vector in pseudo-time is non-linear and is solved by sub-iterations accounting for a stability condition, as shown by Hirsch (Hirsch, 1988) for viscous flow calculations. The generalised conjugate gradient (GCG) is employed to solve the resulting linear system. A block incomplete lower-upper preconditioner is used in this context.

The connectivity between the different grids that constitute the final computational mesh is computed using the Chimera technique. The approach adopted in ROSITA is derived from the one originally proposed by Chesshire and Henshaw (Chesshire and Henshaw, 1990), with some modifications to further improve robustness and performance of the schema. During the tagging procedure, the domain boundaries with solid wall conditions are firstly identified and all points in overlapping grids that fall close to these boundaries are marked as holes (seed points). Then, an iterative algorithm identifies the donor and fringe points and lets the hole points grow from the seeds until they entirely fill the regions outside the computational domain. Oct-tree and alternating digital tree data structures are employed in order to speed up the search of donor points.

When two or more overlapping surface grids are present in the nested grid system, the so-called "zipper-grid" technique of Chan and Buning (Chan and Buning, 1995) is used. This technique consists in eliminating the overlapped surface cells using triangles to fill the gap. The integration of the aerodynamic loads is performed on the resulting hybrid mesh.

The ROSITA solver is fully capable of running in parallel on large computing clusters. The parallel algorithm is based on the message passing programming paradigm and the parallelisation strategy consists in distributing the grid blocks among the available processors. Each grid block can be automatically subdivided into smaller blocks by the solver to obtain an optimal load balancing. Numerical computations were carried out at DAER on the Kelvin cluster, made up of 2 quad-processor sixteen-core AMD® Opteron 6386SE at 2.8 GHz with 256 GB RAM each interconnected by a Qlogic QDR Infiniband high-performance network with capacity of 40 Gb/s.

Since the motion of the oscillating airfoil is periodic and can be prescribed at the very beginning of the numerical simulations, the tagging procedure can be performed in advance on a single complete airfoil

9

oscillation using a parallel algorithm and stored to be retrieved during the actual calculation.

3.2. Numerical model

The numerical model of the oscillating airfoil and the upstream vortex generator in the wind tunnel test section was composed by a total number of four Cartesian multi-block grids that were mounted together using the Chimera technique. The nested grid system consisted of a background mesh representing the wind tunnel, two different meshes for the vortex generator airfoil and the oscillating airfoil (OG) and a higher-resolution mesh for the vortex structure (VG) generated by the upstream vortex generator. A sketch of the airfoils and vortex grids inside the wind tunnel is presented in Fig. 4.
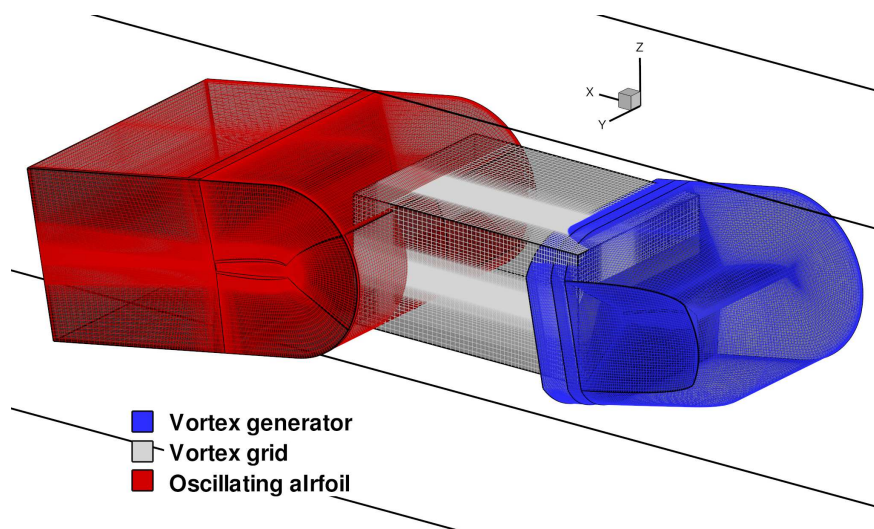

Figure 4: Layout of the nested three-dimensional grid system employed for the numerical analysis of the perpendicular BVI.

The numerical model of the wind tunnel represented a straight duct that was obtained extruding fore and aft the test section (where the oscillating airfoil was placed). In particular, the inflow section of the wind tunnel was placed at a distance of $11.75\ c$ from the origin of the reference system, while the outflow section was located at $20.75\ c$ from the same reference point. With the aim of keeping the computational effort of the simulations suitable with respect to the available resources, the boundary layer on the wind tunnel walls was not reproduced, thus a slip boundary condition was applied on the wind tunnel walls. Nevertheless, significant effects were not expected from this simplification. In fact, simulations of oscillating airfoil experiments carried out with the resolution of the wind tunnel walls boundary layer have not given conclusive results (Klein et al., 2012). However, in order to account the boundary layer effects on the oscillating airfoil tips, the cross section of the wind tunnel was reduced from the actual dimension of $1\ m \times 1.5\ m$ to an equivalent dimension of $0.984\ m \times 1.484\ m$, corresponding to an offset equal to the boundary layer displacement thickness measured for the considered flow velocity (for further details, see Garbaccio

(2011) MSc dissertation). The background mesh was discretised with a H topology and was composed by a total number of 1932000 elements. In stream-wise direction, elements were clustered in the region where the oscillating airfoil and the vortex generator were located. The oscillating airfoil, the vortex generator and the vortex grid were contained inside the background mesh. To allow for a correct execution of the tagging procedure, these grids were created with similar spatial resolution at their outer edges. Both the oscillating airfoil and the vortex generator grids were meshed with a C-H topology with a high element density close to the body surfaces and an increasing stretching away from their surfaces. The minimum spacing in the direction normal to the airfoils surfaces corresponds to $3.33\ c \times 10^{-5}$ and was chosen so that the dimensionless wall distance y^+ of the first layer of cells was less than 1. A no-slip boundary condition was applied on both oscillating airfoil and vortex generator surfaces. The outer boundaries of both grids were at $1\ c$ from the upper and lower surfaces. A small gap between the oscillating airfoil tips and the wind tunnel walls was present, as in the experimental set up. In those regions, the oscillating airfoil mesh was extended up to the wind tunnel walls with a spatial cells distribution designed to match the elements of the background grid. On the other hand, the vortex generator root section lied on the wind tunnel wall. To be able to reproduce this configuration (no gap between different surfaces), the zipped-grid technique (Chan and Buning, 1995) was used on overlapping surface grids. The oscillating airfoil grid was extended up to $2.5\ c$ from the trailing edge while the vortex generator grid was extended up to $0.7\ c$ from the trailing edge. The reduced extension of the latter grid in the trailing edge region was due to the fact that a separated vortex grid (VG) was included in the overset grid system and used to keep the integrity of the stream-wise vortex (Garmann and Visbal, 2015) produced by the vortex generator toward the oscillating airfoil.

In order to investigate the effects of the grids spatial resolution for the analysis of the perpendicular BVI problem, different meshes on the same grid geometry and topology were created with different cell densities. In particular, two meshes were built for the vortex grid (VG1 and VG2) while three meshes were created for the oscillating airfoil (OG1, OG2 and OG3). Details of different meshes are reported in Tab. 1 for the vortex grid and in Tab. 2 for the oscillating airfoil. On the other hand, a unique grid was built for the vortex generator airfoil with the same surface discretisation and near-body elements spacing of the OG2 but with a total number of $1\,816\,452$ elements.

Mesh	N_{Tot}	N_X	N_Y	N_Z	ΔX ($\times 10^{-3}$)	ΔY ($\times 10^{-3}$)	ΔZ ($\times 10^{-5}$)
VG1	$1\,900\,356$	200	82	40	1.70	3.46	3.33
VG2	$3\,003\,465$	270	110	60	1.33	3.33	3.33

Table 1: Details of the vortex grid (minimum spacing are reported in terms of blade section model chord c).

Since the operative condition of the wind tunnel was characterised by a low free stream Mach number ($M_a = 0.09$), numerical computations were carried out using the Turkel's low Mach number preconditioner

Mesh	N_{Tot}	N_ξ	N_ζ	N_η	$\Delta\xi$ $(\times 10^{-3})$	$\Delta\zeta$ $(\times 10^{-3})$
OG1	1 641 476	200	82	40	1.70	3.46
OG2	3 499 372	270	110	60	1.33	3.33
OG3	7 093 800	350	128	80	0.47	3.29

Table 2: Details of the oscillating airfoil grid (minimum spacing are reported in terms of blade section model chord c).

(Turkel et al., 1997). The time-accurate simulations were carried out over a series of successive cycles. Since a dual-time formulation was implemented in ROSITA for the time advancement, a number of 140 pseudo time-steps was used for each real time-step. Numerical results were extracted after three full cycles to ensure a periodic state of the solution. The solutions were achieved by running the ROSITA solver in parallel on 128 processors using a Courant-Friedrichs-Lewy (CFL) number of 3.0.

4. Results and Discussion

The present activity investigated the interactions of a stream-wise vortex impacting on a oscillating airfoil in light dynamic stall condition (McCroskey, 1981). The light dynamic stall cycle considered in this work corresponds to a sinusoidal pitching motion with a mean angle of attack $\alpha_m = 5°$, a constant oscillation amplitude $\alpha_a = 10°$, and a reduced frequency $k = 0.1$. The free-stream velocity was $U_\infty = 30$ m/s corresponding to a Reynolds number (Re) based on airfoil chord of 600 000 and a Mach number (M_a) of 0.09.

In the present study, the upstream vortex generator airfoil was fixed to $\alpha = 10°$. Its vertical and span-wise position was differently adjusted for each considered phase of the pitching cycle selected for this study so that the tip vortex impacts on the target airfoil's leading edge on the wind tunnel mid-plane. In order to highlight the effect of the pitching motion on the vortex interaction, the numerical simulations were performed for two experimental test cases with the vortex impacting on the target airfoil's leading edge at the same angle of attack $\alpha = 10°$ in upstroke and in downstroke phases of the oscillation cycle. As previously explained, although the target airfoil angle of attack was the same for the two considered conditions, the setting of the vortex generator airfoil had to be different for these two phases in order to have the desired vortex impact position despite the wandering produced by the target airfoil oscillation.

4.1. Grid dependence and time step dependence studies

A grid dependence study was carried out for the vortex grid (VG) by means of steady state simulations performed over the two meshes built with different spatial resolution, namely VG1 and VG2 (see Tab. 1). The steady state simulations were performed with the vortex generator airfoil only set at $\alpha = 10°$ to evaluate the capability to reproduce the isolated vortex in the wind tunnel. Figure 5 shows the results of the simulations carried out with the different vortex grids.
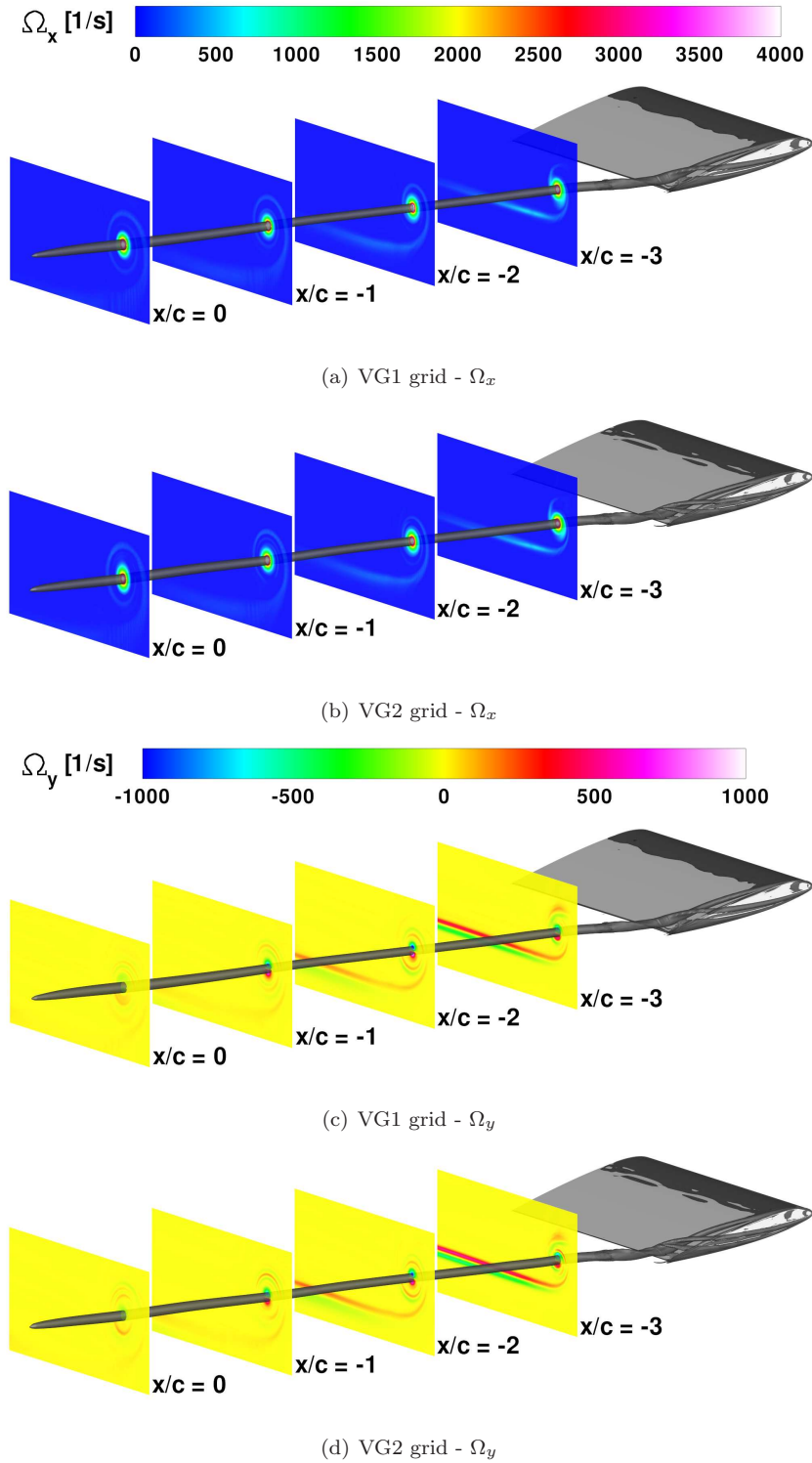
(a) VG1 grid - Ω_x

(b) VG2 grid - Ω_x

(c) VG1 grid - Ω_y

(d) VG2 grid - Ω_y

Figure 5: Steady CFD simulations results for the isolated vortex with different grid resolutions, vortex generator airfoil at $\alpha = 10°$ ($R_e = 6 \cdot 10^5$, $M_a = 0.09$): vorticity components contours on Y-Z planes and iso-surface of q-criterion, $Q = 1.3 \times 10^6 [1/s^2]$ (Hunt et al., 1988)

13

As can be observed, the vorticity components contours show negligible differences between the solutions obtained with the different grid resolution. From the same figure, it is possible to argue that the wake reaching the target airfoil's leading edge position ($x/c = 0$) was limited to the stream-wise vortex structure. In fact, the remaining vortex sheet was characterised by a very low vorticity intensity and in any case was passing below the height of the target airfoil. A quantitative analysis of the grid dependence of the solutions is reported in Fig. 6 showing the comparison of the velocity component profiles extracted through the isolated vortex core on the Y-Z plane positioned in correspondence of the oscillating airfoil leading edge position ($x/c = 0$). The position of the vortex core centre (Y_v,Z_v) corresponds to the position of the maximum of the vorticity magnitude on the selected plane. In this figure, the CFD velocity profiles are compared to the mean velocity profiles measured by stereo PIV surveys (averaged over 100 image pairs) carried out for the same isolated vortex configuration.

(a) v velocity component
(b) w velocity component

Figure 6: Comparison of the velocity profiles extracted through the isolated vortex core on Y-Z plane at $X = 0$ (oscillating airfoil's leading edge position).

The velocity profiles comparison shows that both the CFD solution capture very well the slope of the experimental profiles curves inside the viscous core of the isolated vortex. Small differences between the CFD solutions can be appreciated for the peaks of the velocity components. Also the vortex core location and the viscous radius computed by the two grids are quite similar. Indeed, on the plane at $x/c = 0$ the span-wise and vertical differences between the vortex core centre positions computed with VG1 and VG2 grid are respectively 0.4% and 0.2% of the airfoil chord. Moreover, the vortex core radius, calculated as the radial distance from the vortex core center where the computed tangential velocity has its maximum value, is respectively 18.3 mm and 17.9 mm for the VG1 and VG2 grid. These values are slightly higher than the vortex core radius of 15.8 mm evaluated by hot-wire anemometry surveys performed in the previous work

Time-step	C_{L^w}	C_{D^w}	C_{M^w}
200	0.934	0.063	-0.035
400	0.940	0.061	-0.036
600	0.949	0.061	-0.036

Table 3: CFD results of the time-step dependence study carried out with the oscillating airfoil grid OG2: aerodynamic loads acting on the entire oscillating airfoil span at $\alpha = 10°$ in upstroke with the vortex impacting at the leading edge.

by Gibertini et al. (2014) for the qualification of the same isolated stream-wise vortex. In particular, the hot-wire measurements carried out on the same plane at $x/c = 0$ showed that the vortex has a circulation of about 2.8 m^2/s, slightly lower than the ones computed by numerical simulations (about 2.9 m^2/s). This analysis shows that the spatial discretisation of the VG1 can be considered enough to obtain a correct representation of the impacting vortex, keeping at the same time the computational burden at an acceptable level considering the available resources.

A time-step and a grid dependence study was also carried out for the CFD solution with the vortex impacting on the oscillating airfoil. In particular, these studies were performed for the test case with the vortex impacting on the leading edge of the oscillating airfoil at $\alpha = 10°$ in upstroke.

Time-accurate simulations were carried out with different time-steps per period using the OG2 for the oscillating airfoil.

The results of the time-step dependence assessment in terms of the flow field are presented in Fig. 7. The vorticity magnitude contours plotted on several Y-Z planes and the impacting vortex structure illustrated by the iso-surface of q-criterion show negligible difference between the solutions computed with different time resolutions. Moreover, the results of the same CFD simulations in terms of the lift, drag and pitching moment coefficients acting on the entire oscillating airfoil span are reported in Tab. 3, as done in Garmann and Visbal (2015).
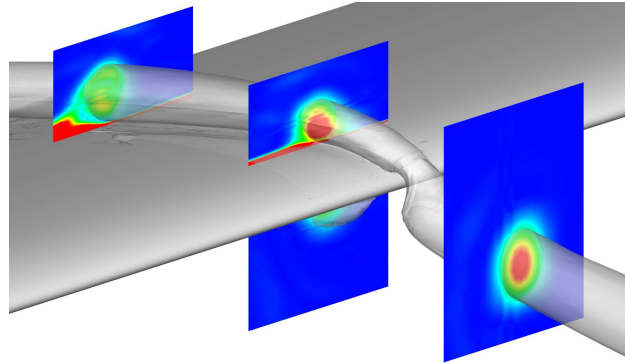
A weak dependence on the time resolution can also be observed for the computed aerodynamic loads, in particular between 400 and 600 TS per period. Therefore, the solution over 400 TS per period provides confidence for the simulation of the perpendicular BVI test cases. Then, this resolution in time was used in the remainder numerical studies performed in the present work.

A spatial dependence study was carried out for the oscillating airfoil grid considering the same test case of the time-step dependence assessment. The comparisons of the flow fields and of the aerodynamic loads computed with 400 TS per period over three grid with different resolution are shown respectively in Fig. 8 and in Tab. 4.
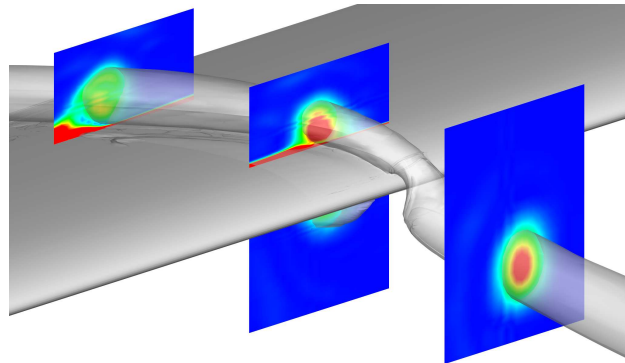
Also for the present study, a weak dependence on the spatial resolution of the oscillating airfoil grid is apparent for both the computed flow fields and the aerodynamic loads. Thus, the grid with intermediate resolution OG2 was used for the remainder numerical simulations.

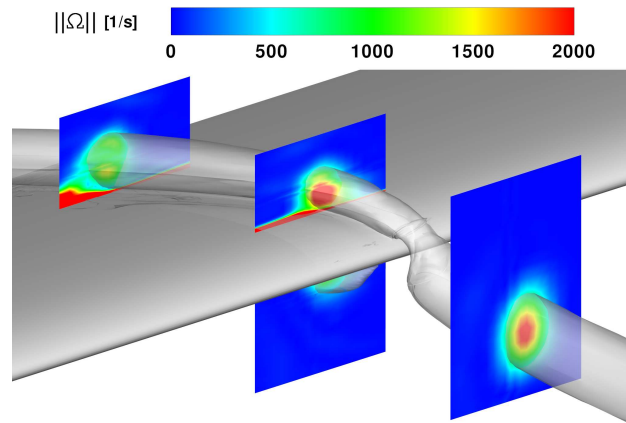15

(a) OG2 grid, 200 TS

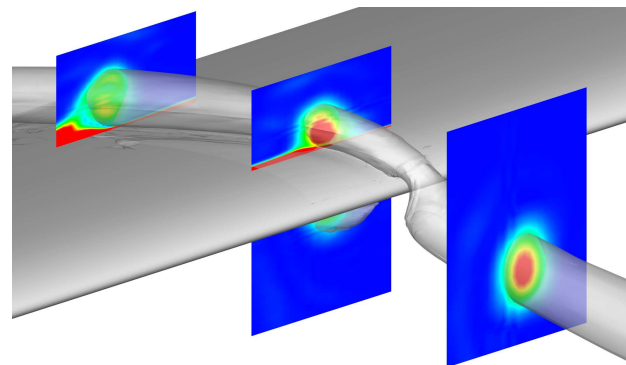(b) OG2 grid, 400 TS

(c) OG2 grid, 600 TS

Figure 7: CFD results of the time-step dependence study carried out with the oscillating airfoil grid OG2: vorticity magnitude contours on Y-Z planes and iso-surface of q-criterion (Hunt et al., 1988), $Q = 15 \times 10^3 [1/s^2]$, at $\alpha = 10°$ in upstroke with the vortex impacting at the leading edge.
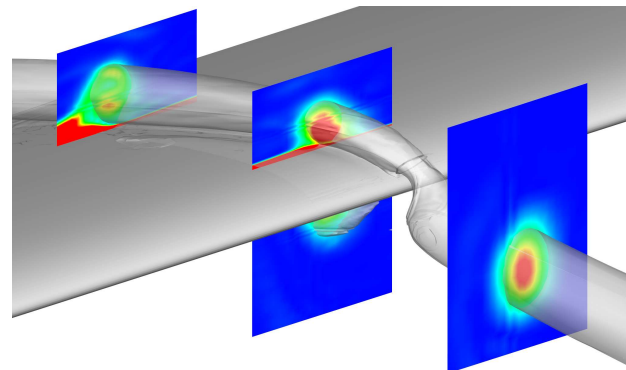
4.2. Flow field analysis

A particular of the CFD solutions presented in Fig. 9 shows the target airfoil's leading edge region stroked by the vortex for the two investigated test conditions ($\alpha = 10°$ upstroke and $\alpha = 10°$ downstroke).

16

(a) OG1 grid, 400 TS

(b) OG2 grid, 400 TS

(c) OG3 grid, 400 TS

Figure 8: CFD results of the spatial dependence study carried out using 400 TS per period: vorticity magnitude contours on Y-Z planes and iso-surface of q-criterion (Hunt et al., 1988), $Q = 15 \times 10^3 [1/s^2]$, at $\alpha = 10°$ in upstroke with the vortex impacting at the leading edge.

The experimental and numerical results were compared to the ones obtained for the same test conditions without the impacting vortex in order to clearly evaluate the influence of the vortex on the performance and

17

Grid	C_{L^w}	C_{D^w}	C_{M^w}
OG1	0.936	0.061	-0.035
OG2	0.940	0.061	-0.036
OG3	0.930	0.061	-0.035

Table 4: CFD results of the spatial dependence study carried out using 400 TS per period: aerodynamic loads acting on the entire oscillating airfoil span at $\alpha = 10°$ in upstroke with the vortex impacting at the leading edge.
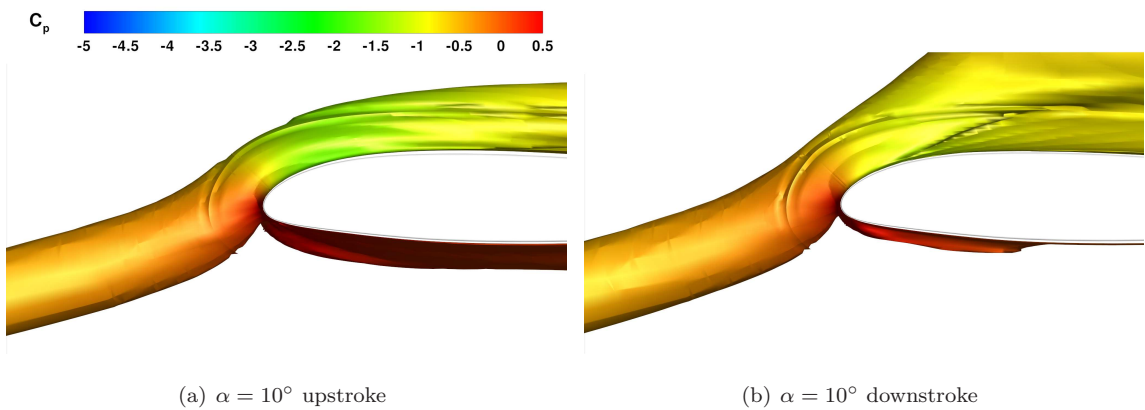
the flow field of the blade.

(a) $\alpha = 10°$ upstroke   (b) $\alpha = 10°$ downstroke

Figure 9: Particular of the CFD solution with the vortex impacting on the oscillating airfoil's leading edge (OG2, 400TS): iso-surface of vorticity magnitude ($\|\mathbf{\Omega}\| = 1 \times 10^3 [1/s]$) colored by pressure coefficient C_P.

Figure 10 shows the u velocity component contours on Y-Z planes at different chord-wise locations for the test case with the oscillating airfoil at $\alpha = 10°$ in upstroke with and without the impacting vortex. Three-dimensional streamlines are plotted on the same figures to show the overall behaviour of the flow field while, for the interacting configuration the iso-surface of q-criterion (Hunt et al., 1988) is illustrated to clearly show the vortex structures.

A quite two-dimensional flow behaviour was observed from both the experimental and numerical results without vortex interaction (see Fig. 10a and b). In particular, the three-dimensional streamlines patterns show a regular flow behaviour above the airfoil upper surface.

For the test case with the interacting vortex, a quite good agreement between the simulations and experiments can be observed for the overall flow field (see Fig. 10c and d). Indeed, the three-dimensional streamlines representation shows that the impacting vortex remains coherent along the target airfoil for both the experiment and the numerical simulation. A larger vortex diameter is visible from simulation results, while the vortex position is quite well predicted, as very small differences in the vortex core location are found over the upper surface region of the oscillating airfoil. For instance, on the plane at $X/c = 0.5$ the

span-wise and vertical differences between the vortex core centre positions evaluated by PIV and CFD are respectively 3% and 0.5% of the airfoil chord. In the present test case, the vertical velocity component induced by the impacting vortex produces a local variation of the oscillating airfoil angle of attack that is decreased for negative Y and increased for positive Y. The numerical flow field shows a contained back-flow region close to the airfoil upper surface towards the trailing edge for positive Y, where the impacting vortex induces a conspicuous increase of the local angle of attack. In particular, the vortex convects progressively towards the positive Y direction according to its sense of rotation, as typically observed for a vortex in proximity of a wall. A quite regular behaviour of the flow can be observed outside the vortex region of interest.
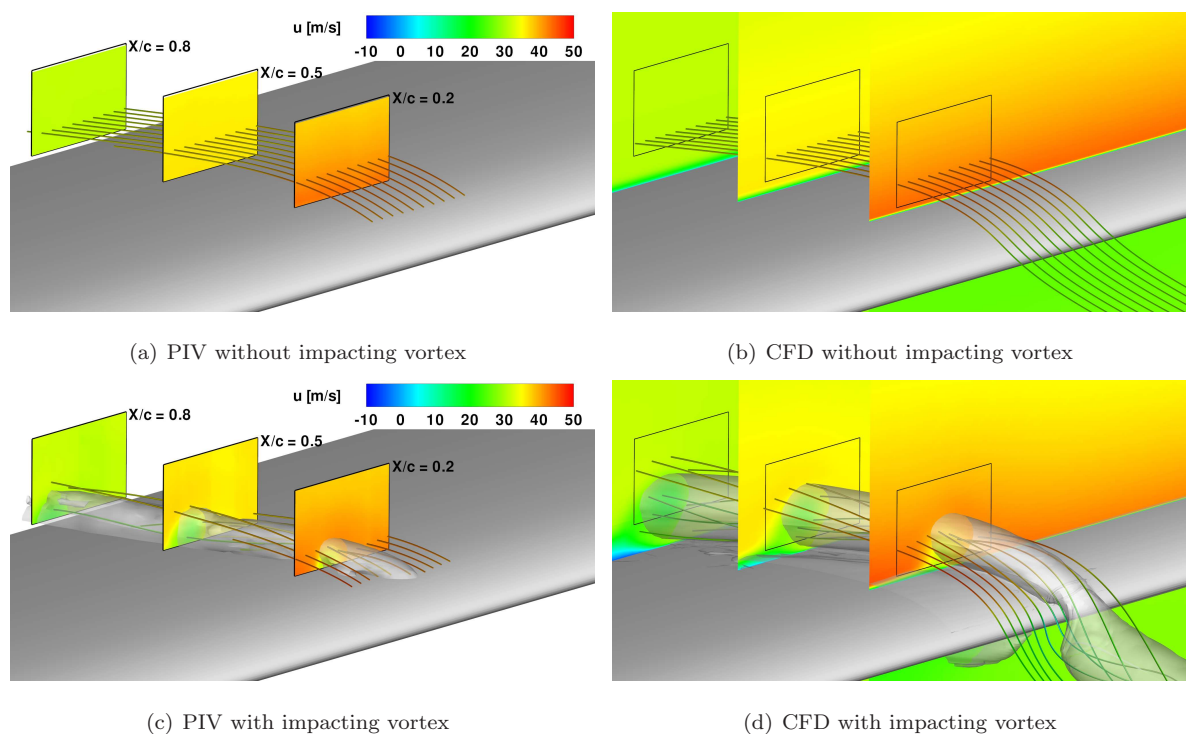

(a) PIV without impacting vortex

(b) CFD without impacting vortex

(c) PIV with impacting vortex

(d) CFD with impacting vortex

Figure 10: Comparison of PIV/CFD results for test case with the target airfoil at $\alpha = 10°$ in upstroke (Re $= 6 \times 10^5$, Ma $= 0.09$): u velocity component contours on Y-Z planes and three-dimensional streamlines colored by u. The iso-surface of the q-criterion (Hunt et al., 1988) is plotted for the case with impacting vortex both in PIV and CFD results ($Q = 15 \times 10^3 [1/s^2]$).

A quantitative comparison between PIV and CFD velocity fields is reported in Fig. 11 for the interacting case, showing the u velocity profiles extracted at three different span-wise positions on two Y-Z planes along the oscillating airfoil chord. A quite good agreement between experimental and numerical results can be observed for the velocity profiles extracted on both the selected Y-Z planes, confirming the reliability of the numerical solution.

The numerical and experimental flow fields for the test case with the oscillating airfoil at $\alpha = 10°$ in

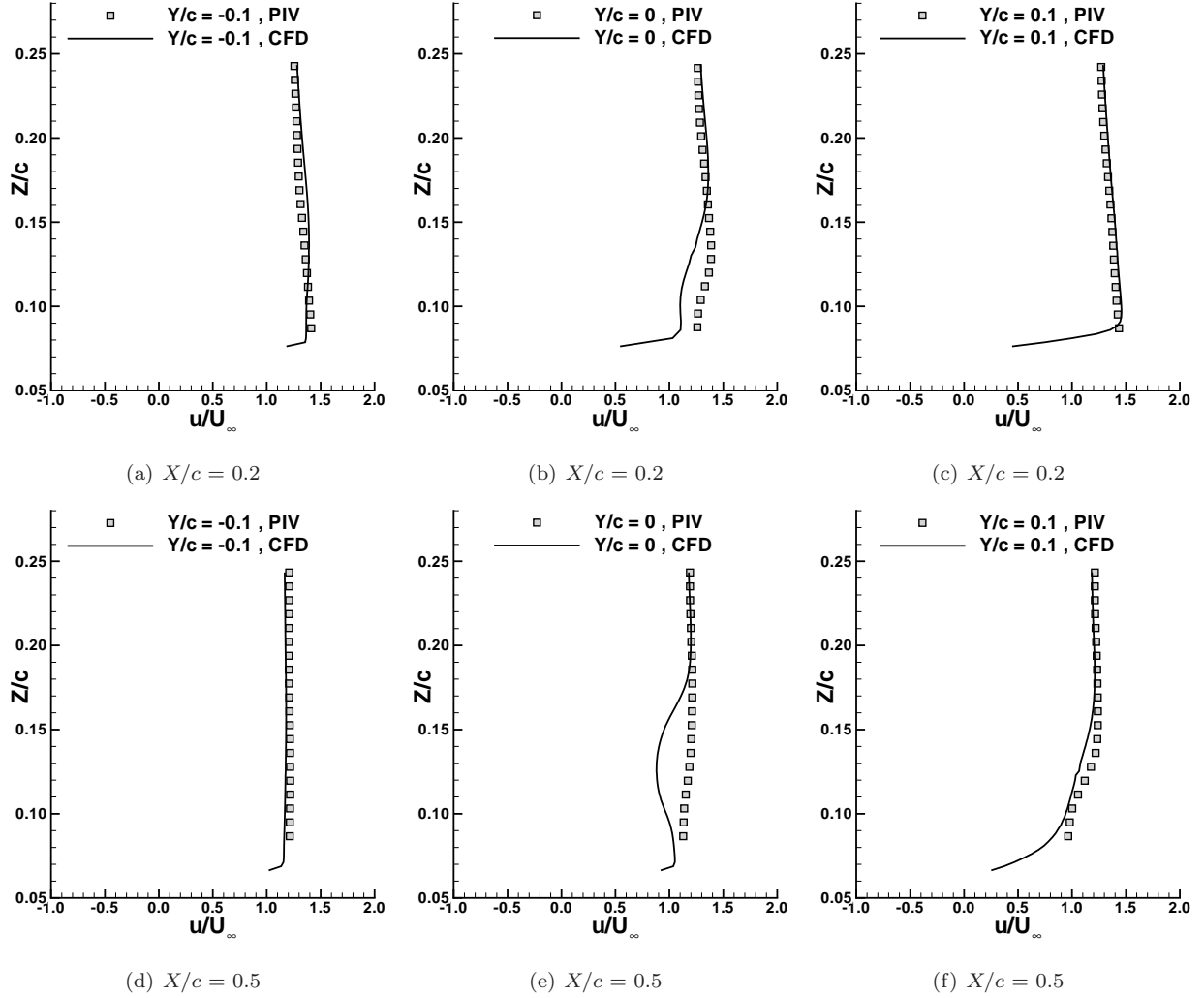Figure 11: Comparison of PIV/CFD results for the interacting test case with the target airfoil at $\alpha = 10°$ in upstroke (Re = 6×10^5, Ma = 0.09): u velocity profiles extracted on Y-Z planes.

downstroke are shown in Fig. 12. Analogously to what observed for the corresponding angle of attack of the oscillating airfoil in upstroke, the streamlines representation obtained from PIV and CFD results at $\alpha = 10°$ in downstroke without the impacting vortex shows an regular flow behaviour above the airfoil upper surface (see Fig. 12a and b), as can be expected for the light dynamic stall regime.

For the interacting case, the upward velocity component induced by the vortex towards positive Y produced a large back-flow region on the airfoil upper surface. This different behaviour of the interacting flow field with respect to the test case at the same angle of attack in upstroke could be explained by the contributory kinematic effect induced by the rapid negative pitching rate of the airfoil (McCroskey, 1981; Leishman, 2000). This effect, comparable to a modification of the airfoil camber, promotes the local stall onset in this phase of the pitching motion. The overall high chaotic behaviour of the experimental flow field

20

is captured by the numerical simulation, even if a larger back-flow region in the region of the PIV survey can be observed from CFD results (see Fig. 12c and d). The three-dimensional streamlines representation shows that this region is characterised by a strongly three-dimensional recirculating region overstepped by the flow coming from the fore region. Moreover, both CFD simulation and PIV results show that the impacting vortex looses its coherence just aft the leading edge region, as highlighted by the iso-surface of q-criterion.
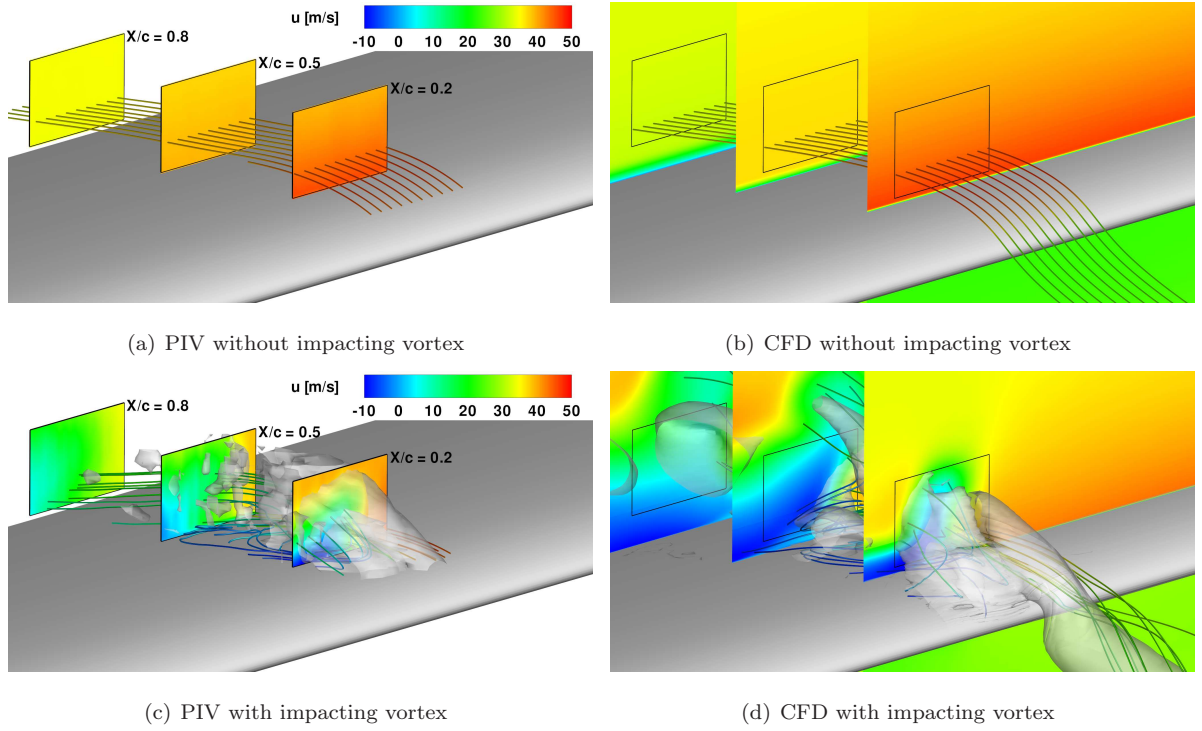

(a) PIV without impacting vortex

(b) CFD without impacting vortex

(c) PIV with impacting vortex

(d) CFD with impacting vortex

Figure 12: Comparison of PIV/CFD results for test case with the target airfoil at $\alpha = 10°$ in downstroke (Re = 6×10^5, Ma = 0.09): u velocity component contours on Y-Z planes and three-dimensional streamlines colored by u. The iso-surface of the q-criterion (Hunt et al., 1988) is plotted for the case with impacting vortex both in PIV and CFD results ($Q = 1 \times 10^5 [1/s^2]$).

The comparison of the u velocity component profiles presented in Fig. 13 for the interacting case shows a good agreement of the experimental and numerical results for the Y-Z plane at $X/c = 0.2$. Higher discrepancies can be observed from the comparison of the velocity profiles extracted on the Y-Z plane at $X/c = 0.5$. Nevertheless, a certain degree of disagreement between the simulation results and averaged measurements can be reasonably expected in presence of massive separation and high flow unsteadiness, as also found in other recent activities regarding the numerical simulation of similar flow features, i.e deep dynamic stall regime over an oscillating airfoil (Costes et al., 2015; Kaufmann et al., 2015; Zanotti et al., 2014b). Moreover, the results of the statistical convergence study performed over the collected PIV data set (see Sec. 2.2) suggested that the choice of 100 image pairs for the phase-average process of the PIV data should not have remarkable effects on the discrepancies observed in the comparison of the streamwise
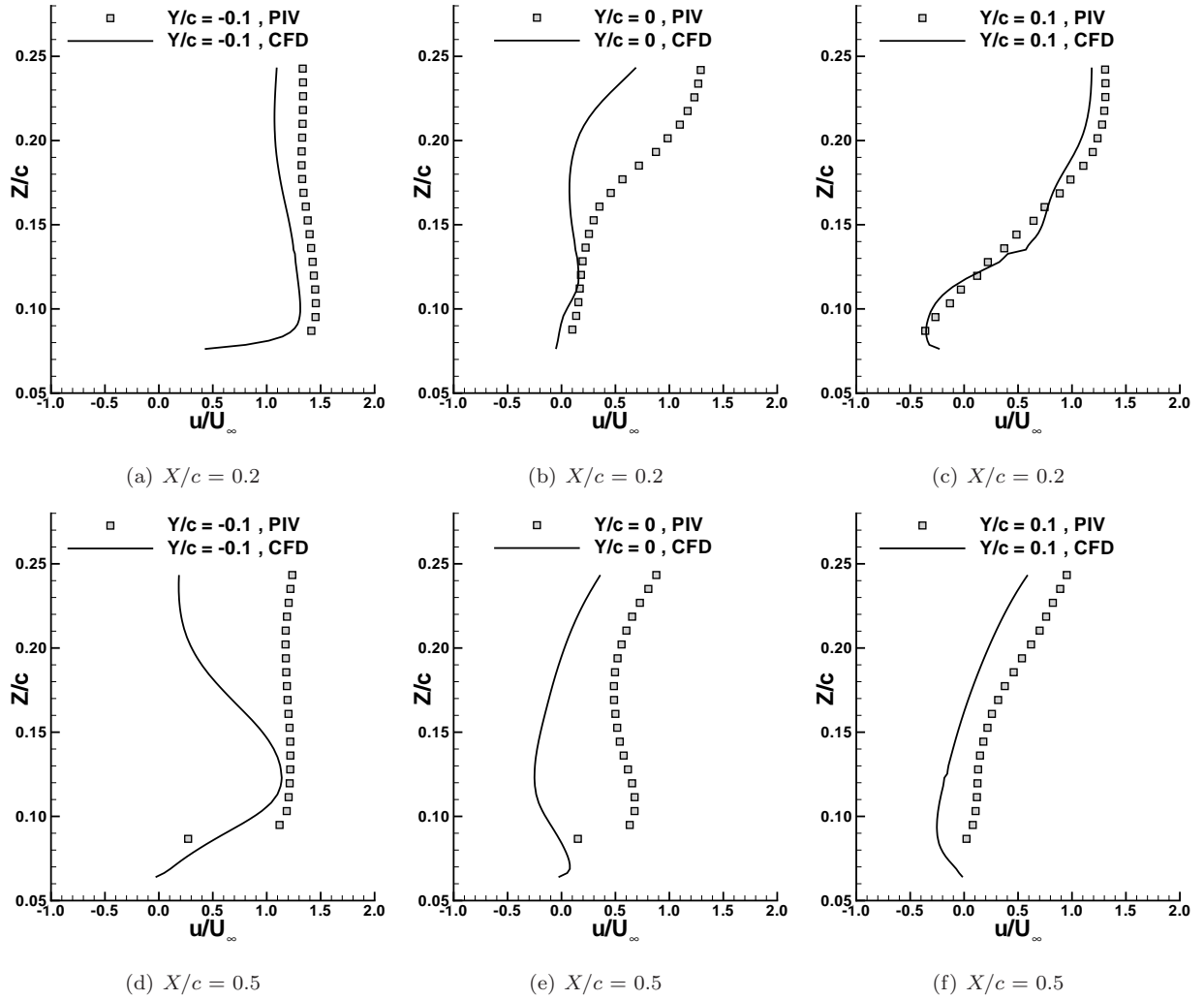
velocity profiles for this test case.

Figure 13: Comparison of PIV/CFD results for the interacting test case with the target airfoil at $\alpha = 10°$ in downstroke (Re $= 6 \times 10^5$, Ma = 0.09): u velocity profiles extracted on Y-Z planes.

The CFD solutions were then used to provide an analysis of the flow features evolution along the whole oscillating cycle. Figures 14 and 15 show the isosurface of q-criterion (Hunt et al., 1988), computed with a constant step of 5° along the cycle, respectively for the two test conditions with the vortex impacting on the oscillating airfoil's leading edge at $\alpha = 10°$ upstroke and downstroke.
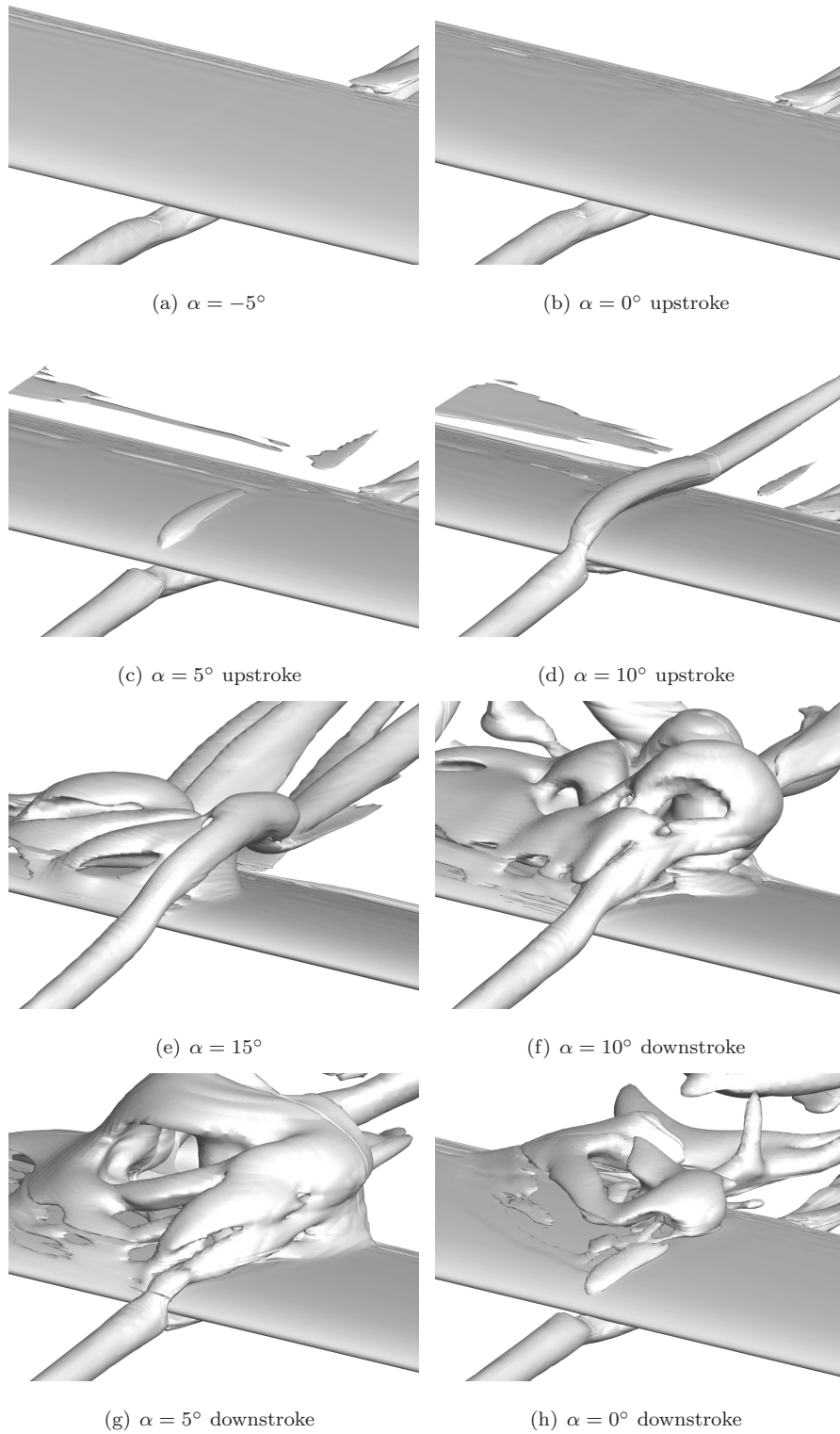
(a) $\alpha = -5°$ (b) $\alpha = 0°$ upstroke

(c) $\alpha = 5°$ upstroke   (d) $\alpha = 10°$ upstroke

(e) $\alpha = 15°$ (f) $\alpha = 10°$ downstroke

(g) $\alpha = 5°$ downstroke   (h) $\alpha = 0°$ downstroke

Figure 14: CFD results for test case with the vortex impacting at the target airfoil's leading edge for $\alpha = 10°$ in upstroke (Re $= 6 \times 10^5$, Ma $= 0.09$): iso-surface of the q-criterion (Hunt et al., 1988) ($Q = 15 \times 10^3 [1/s^2]$).
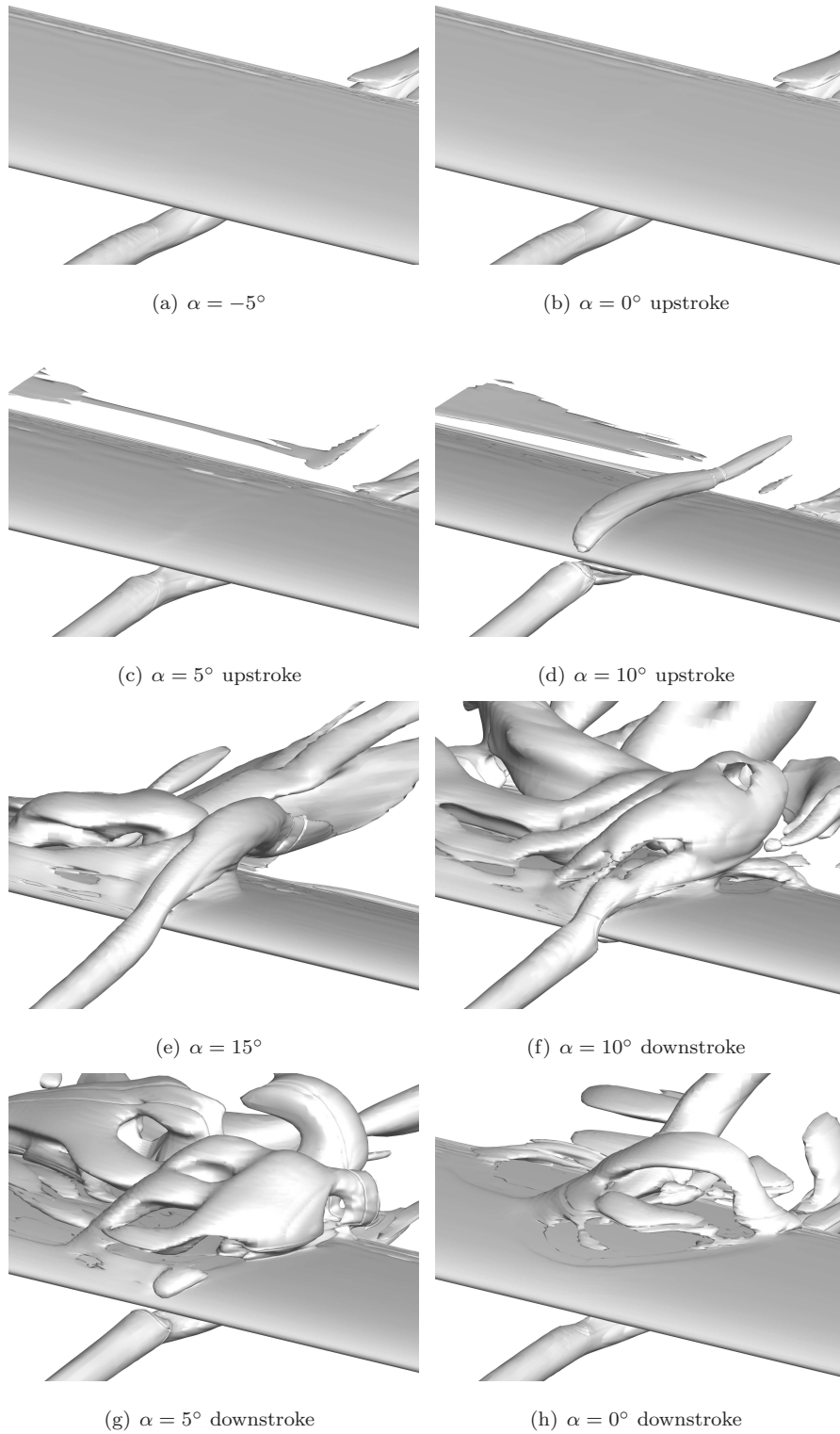
23

(a) $\alpha = -5°$

(b) $\alpha = 0°$ upstroke

(c) $\alpha = 5°$ upstroke

(d) $\alpha = 10°$ upstroke

(e) $\alpha = 15°$

(f) $\alpha = 10°$ downstroke

(g) $\alpha = 5°$ downstroke

(h) $\alpha = 0°$ downstroke

Figure 15: CFD results for test case with the vortex impacting at the target airfoil's leading edge for $\alpha = 10°$ in downstroke (Re $= 6 \times 10^5$, Ma $= 0.09$): iso-surface of the q-criterion (Hunt et al., 1988) ($Q = 15 \times 10^3 [1/s^2]$).

For the first test case, the vortex at $\alpha = -5°$ passes under the oscillating airfoil, as can be clearly observed in Fig. 14a. Then, in upstroke motion the vortex arises remaining under the oscillating airfoil at $\alpha = 0°$ (see Fig. 14b). At $\alpha = 5°$ in upstroke the vortex structure brushes the lower airfoil surface (see Fig. 14c). Then it strokes the airfoil leading edge at $\alpha = 10°$ (see Fig. 14d). The upward motion of the vortex structure is produced by the induction of the oscillating airfoil circulation associated to the lift and to the nose-up rotation about its quarter of chord. In the remaining part of the upstroke motion, the vortex is deflected further upward. Indeed, at the maximum incidence $\alpha = 15°$ the vortex structure is over the oscillating airfoil upper surface maintaining its coherence (see Fig. 14e). However, at this attitude the vortex is responsible of the local stall onset occurring for positive Y where it induces an upward velocity, as can be clearly observed from the high chaotic behaviour illustrated by the q-criterion iso-surface. This flow behaviour is apparent on the whole downstroke motion due to the rapid negative pitching rate of the airfoil that, as previously mentioned, promotes the local stall (McCroskey, 1981; Leishman, 2000). In particular, an emphasised chaotic flow is observed at $\alpha = 10°$ in downstroke, where the effect of the vortex is more pronounced as, moving downward, it approaches the upper surface of the airfoil (see Fig. 14f) and then at $\alpha = 5°$ it is splitted almost simmetrically by the airfoil's leading edge (see Fig. 14g). At $\alpha = 0°$ in downstroke, a part of the vortex is still on the upper side of the oscillating airfoil (see Fig. 14h) producing a more contained effect on the local flow field behaviour. Moreover, it must be pointed out that in downstroke phase the vortex attitude presents a slightly higher upward deflection with respect to the upstroke phase.

For the second test case, the evolution of the vortex structure resumes similar characteristics with respect to the first test case. In general, the same very similar phenomena can be observed along the oscillation cycle but at different angles of attack. In fact, for example at $\alpha = 10°$ in downstroke (see Fig. 15f), when the vortex impacts the leading edge in this test case, the flow behaviour is quite similar to what observed at $\alpha = 5°$ in downstroke in the previous case.

The different behaviour of flow features observed for both the test cases during the motion of upstroke and downstroke makes expectable a conspicuous hysteresis of the sectional airlods acting on the oscillating airfoil for positive Y, as it occurs for deep dynamic stall regime (McCroskey, 1981).

The CFD solutions were then used to provide an analysis of the flow field over the entire oscillating airfoil span, particularly for the phases of the oscillation cycle where the stream-wise vortex is made purposely to impact at the airfoil's leading edge. In particular, the contours of the skin friction coefficient C_f on the upper surface of the oscillating airfoil are shown in Figs. 16 and 17 respectively for the test case with the vortex impacting on the airfoil's leading edge at $\alpha = 10°$ in upstroke and downstroke. The skin friction patterns are plotted on the same figures.

For the test case with $\alpha = 10°$ in upstroke without the vortex interaction a quite two-dimensional behaviour of the flow can be observed, with a contained separated region confined towards the trailing edge of the oscillating airfoil (see Fig. 16a). In the interacting case, a region of separated flow can be observed

25

where the impacting vortex induces an upward velocity. This region with a small extent starts from the quarter of the airfoil chord and is confined to the area where the vortex strokes the airfoil (see Fig. 16b). Moreover, an increase of the skin friction can be observed in the region where the vortex induces a downward velocity as well as at the tips of the oscillating airfoil due to the tip vortices.
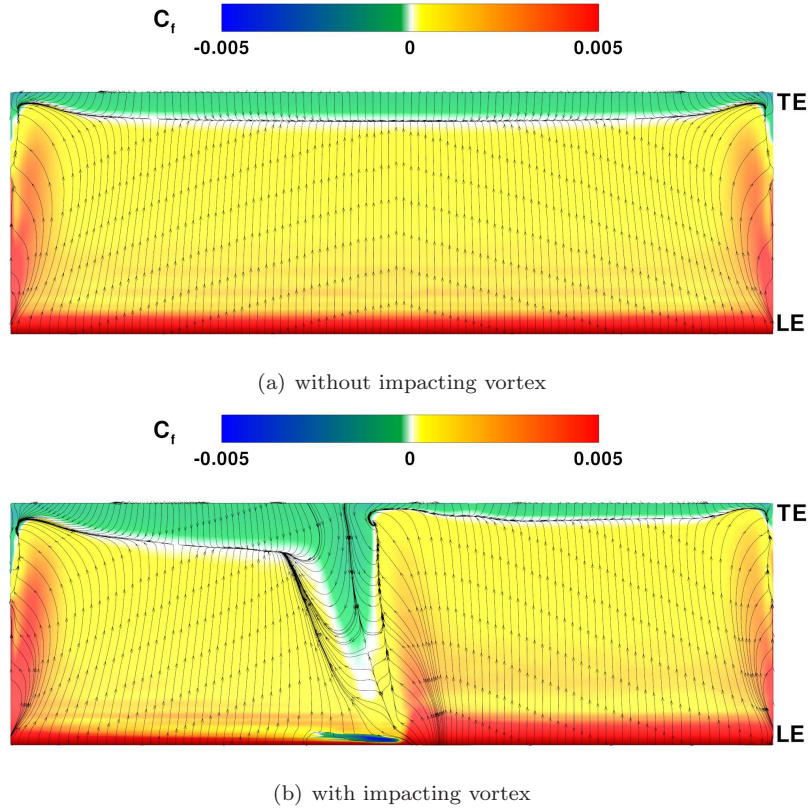

(a) without impacting vortex

(b) with impacting vortex

Figure 16: CFD results for test case with the target airfoil at $\alpha = 10°$ in upstroke (Re $= 6 \times 10^5$, Ma $= 0.09$): skin friction coefficient C_f contours on the oscillating airfoil upper surface.

A behaviour similar to the one observed for the upstroke condition was obtained for the skin friction distribution computed at $\alpha = 10°$ in downstroke without the vortex interaction. In particular, the extent of the separated region towards the oscillating airfoil trailing edge is slightly larger for the downstroke condition (see Fig. 17a). As anticipated by the three-dimensional flow field representation, the most interesting feature is that, in this phase of the motion, the vortex interaction produces a chaotic flow region that involves more than half of the oscillating airfoil suction side, starting from midspan up to the tip (see 17b). Thus, the comparison with the clean case shows that in downstroke motion the vortex interaction influences a wide region of the flow over the blade suction side that could lead to important detrimental effects on the blade performance, as will be analysed in the following section.
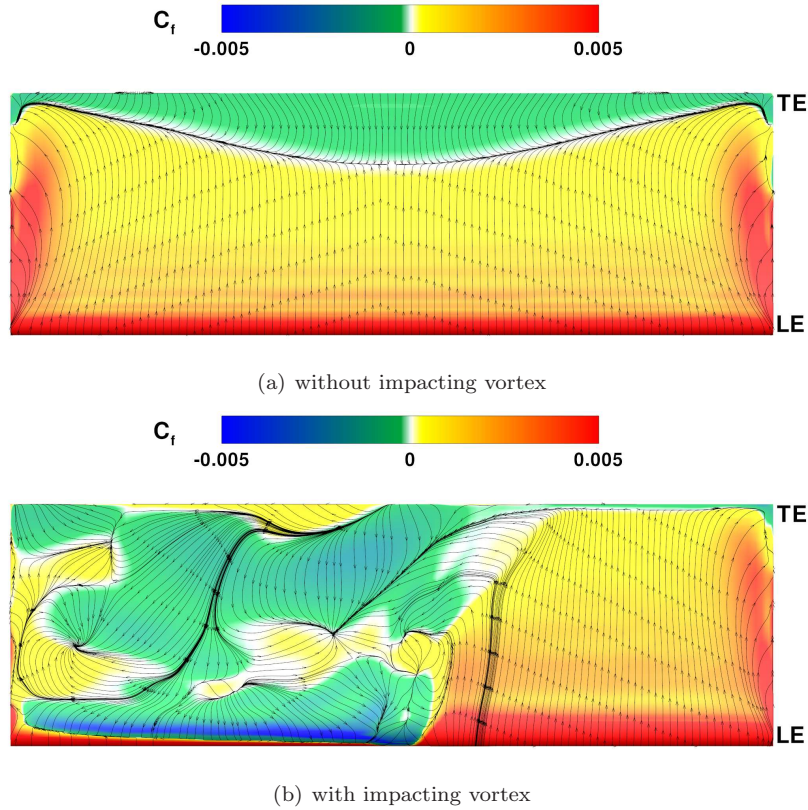
26

(a) without impacting vortex

(b) with impacting vortex

Figure 17: CFD results for test case with the target airfoil at $\alpha = 10°$ in downstroke (Re $= 6 \times 10^5$, Ma $= 0.09$): skin friction coefficient C_f contours on the oscillating airfoil upper surface.

4.3. Aerodynamic performance analysis

The light dynamic stall regime is characterised by minor flow separation on the upper surface of the clean airfoil geometry and by a small amount of aerodynamic loads hysteresis. For the considered oscillation cycle, this feature is clearly shown by the lift and pitching moment coefficients curves evaluated on the midspan section of the oscillating airfoil. In particular, Fig. 18 shows the comparison between the airloads curves computed by CFD simulations carried out for the clean oscillating airfoil geometry and the experimental ones obtained by the integration of pressure measured on the blade section midspan contour. The unsteady pressure measurements were performed in the frame of dynamic stall investigation carried out in Zanotti and Gibertini (2013). In particular, twenty-one fast-response Kulite pressure transducers (2 PSI, FS) were used. The distribution of the pressure taps on the midspan airfoil contour is illustrated in Zanotti and Gibertini (2013). The pressure trasducers signals were collected over 30 complete pitching cycles with a sampling rate of 50 kHz. The phase average of the pressure data was carried out using a bin of 0.1° angle of attack amplitude. A quite good agreement between numerical and experimental airloads curves was obtained for the considered oscillation cycle. This feature gives a further confirmation of the accuracy of

27

the CFD simulation of the present test case.

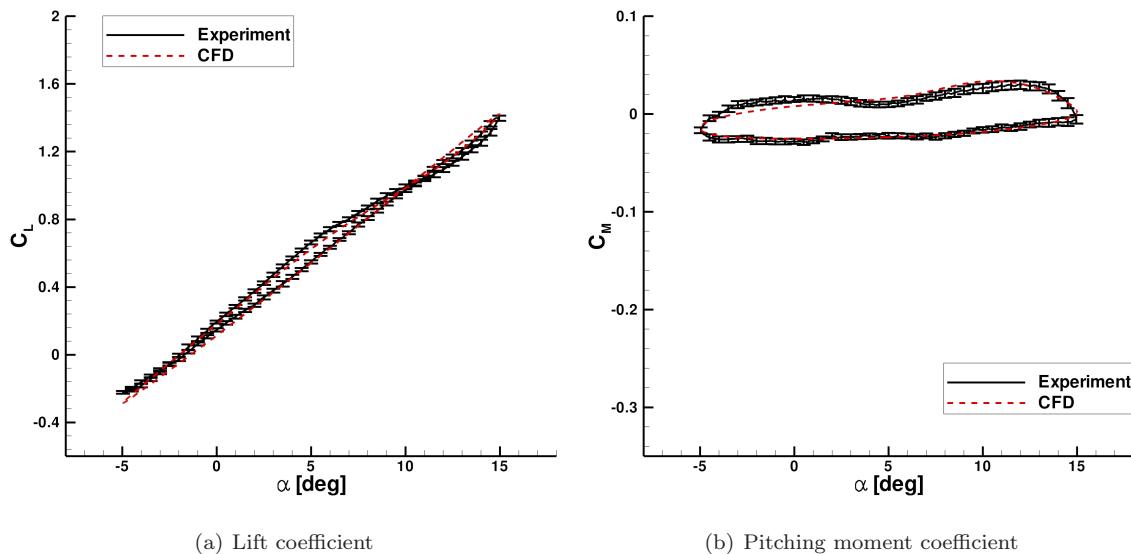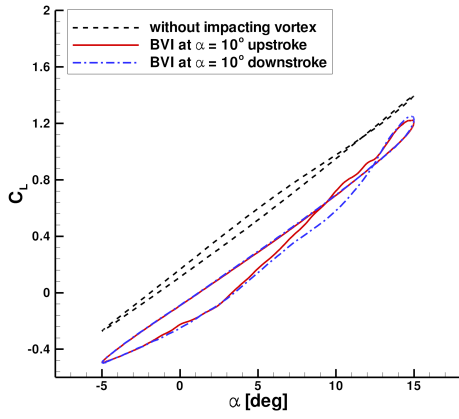(a) Lift coefficient   (b) Pitching moment coefficient

Figure 18: Comparison of the airloads coefficients cycles evaluated at $Y/b = 0$ (midspan section) for the clean oscillating airfoil in light dynamic stall condition ($R_e = 6 \times 10^5$, $M_a = 0.09$). The error bars on the experimental curves represent the standard deviation of the measured airloads coefficients.
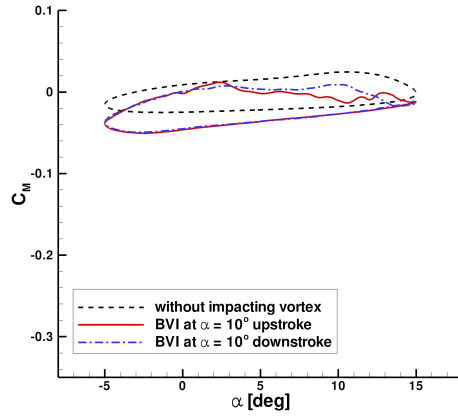
The blade performance analysis was performed by comparing the CFD simulations results obtained with the vortex impacting with the ones obtained for the clean oscillating airfoil geometry. In particular, Fig. 19 shows the comparison of the lift and pitching moment coefficients calculated for both the considered test cases over three different sections in span-wise direction of the oscillating airfoil.

For the section at $Y/b = -0.25$, the lift and pitching moment cycles calculated for both the interacting cases show a contained amount of hysteresis as calculated for the clean airfoil geometry (see Fig. 19a and b). Nevertheless, the downward velocity induced by the stream-wise vortex for negative Y is responsible for a decrease of the airloads values on this section, even if the slope of the lift curve during the upstroke motion remains quite similar to the one computed for the clean airfoil.
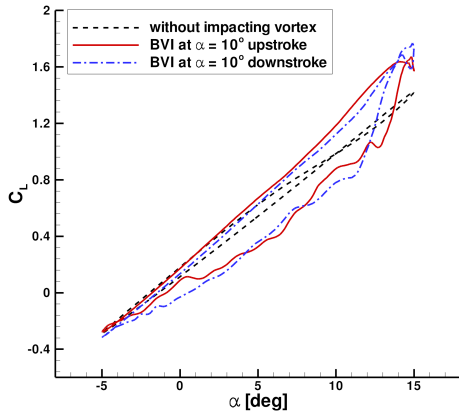
The lift coefficient curves evaluated in upstroke on midspan section ($Y/b = 0$) show, for both the considered interacting cases, a behaviour quite similar to the one calculated for the clean airfoil up to the mean angle of attack of the oscillation cycle. Increasing the angle of attack, an increase of the lift curve slope is observed for both the interacting cases due to the influence of the stream-wise vortex travelling close to the airfoil surface during this part of the oscillation cycle (see Fig. 19c). Even if a benefit in terms of local lift increase is obtained in this part of the motion, the vortex interaction produces on this section a conspicuous increase of the airloads hysteresis, particularly apparent for the pitching moment (see Fig. 19d). In fact, a severe increase of the negative pitching moment peak is observed at the top of the oscillation cycle for both the considered interacting cases. The pitching moment coefficient curves in downstroke are
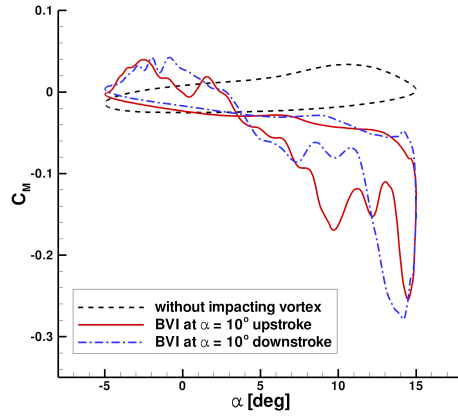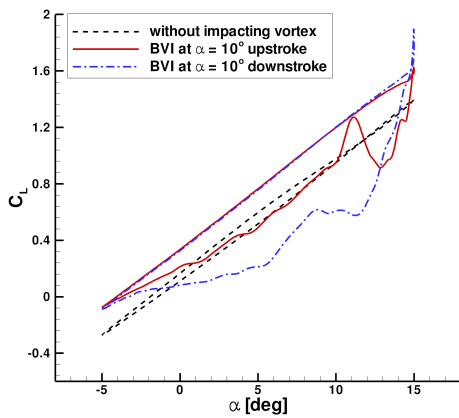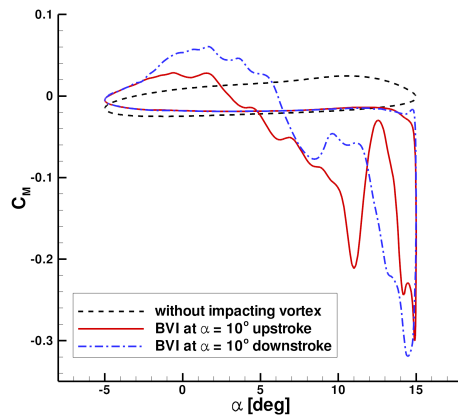
28

(a) $Y/b = -0.25$

(b) $Y/b = -0.25$

(c) $Y/b = 0$

(d) $Y/b = 0$

(e) $Y/b = 0.25$

(f) $Y/b = 0.25$

Figure 19: Comparison of the airloads coefficients cycles computed by CFD at different span-wise section of the oscillating airfoil with vortex interaction ($R_e = 6 \times 10^5$, $M_a = 0.09$).

characterised by rapid overshoots representing a quite adverse effect for blade section structure. Moreover, the most important aspect concerning the vortex interaction is that the clockwise loop area of the pitching moment coefficient curve results to be higher than the anticlock-wise loop one. This feature, producing a net negative aerodynamic damping, could lead to the *stall flutter* occurrence (Carta, 1967) that could produce important structural damages to the blade and a high level of vibrations. Consequently, for the present test cases, the vortex interaction triggers the local stall, as the airloads curves on this section resumes the same characteristics of the deep dynamic stall regime (McCroskey, 1981; Leishman, 2000).

For the section at $Y/b = 0.25$, a positive shift of the lift curves with respect to the clean geometry case is observed during the upstroke motion for both the interacting cases (see Fig. 19e). This feature can be explained with the effect of the local angle of attack increase produced by the upward velocity induced for positive Y by the interacting vortex. A higher amount of the lift curves hysteresis with respect to the clean geometry case can be observed for the interacting cases also on this blade section, particularly apparent for the case with vortex interaction at $\alpha = 10°$ in downstroke. In fact, in this case the impact of the stream-wise vortex triggers the deep stall of the flow over a wide area of the blade upper surface that persists for almost the whole downstroke motion. Consequently, for both the interacting cases, the pitching moment coefficient curves resume a behaviour similar to the ones extracted at midspan section (see Fig. 19f). In particular, relevant peaks and rapid overshoots of the pitching moment occur during the downstroke motion, leading also on this section to the risk of the stall flutter occurrence.

A more detailed insight was dedicated to the phases of the oscillation cycle where the stream-wise vortex is made to impact at the airfoil's leading edge for the two different test cases considered in the present work. The distribution of the aerodynamic loads computed by CFD simulations over the entire oscillating airfoil span for $\alpha = 10°$ in upstroke and in downstroke is presented in Fig. 20. In particular, Fig. 21 shows the comparison of the three-dimensional distribution of the pressure coefficient computed over the upper and lower surface of the oscillating airfoil for the same phases.

For the case with the vortex impacting at $\alpha = 10°$ in upstroke, the comparison with the quite flat behaviour of the lift distribution computed for the clean airfoil (except for the tip regions) shows that the vortex interaction does not produce an appreciable variation of the integral lift force acting on the entire blade span. In fact, the lift increase produced for positive Y is almost similar to the lift decrease induced by the vortex for negative Y (see Fig. 20a). The same considerations are valid for the pitching moment distribution showing, in particular, small fluctuations around the midspan region where the vortex strokes the airfoil's leading edge (see Fig. 20b).

For this interacting case the C_P distribution on the airfoil upper surface shows a conspicuous increase of the suction peak with respect to the clean geometry case in the region where the impacting vortex induces an upward velocity and a drop where a downward velocity is induced by the vortex interaction (see Fig. 21a and b). However, a regular chord-wise distribution of the C_P is observed for the interacting case as for

(a) $\alpha = 10°$ upstroke

(b) $\alpha = 10°$ upstroke

(c) $\alpha = 10°$ downstroke
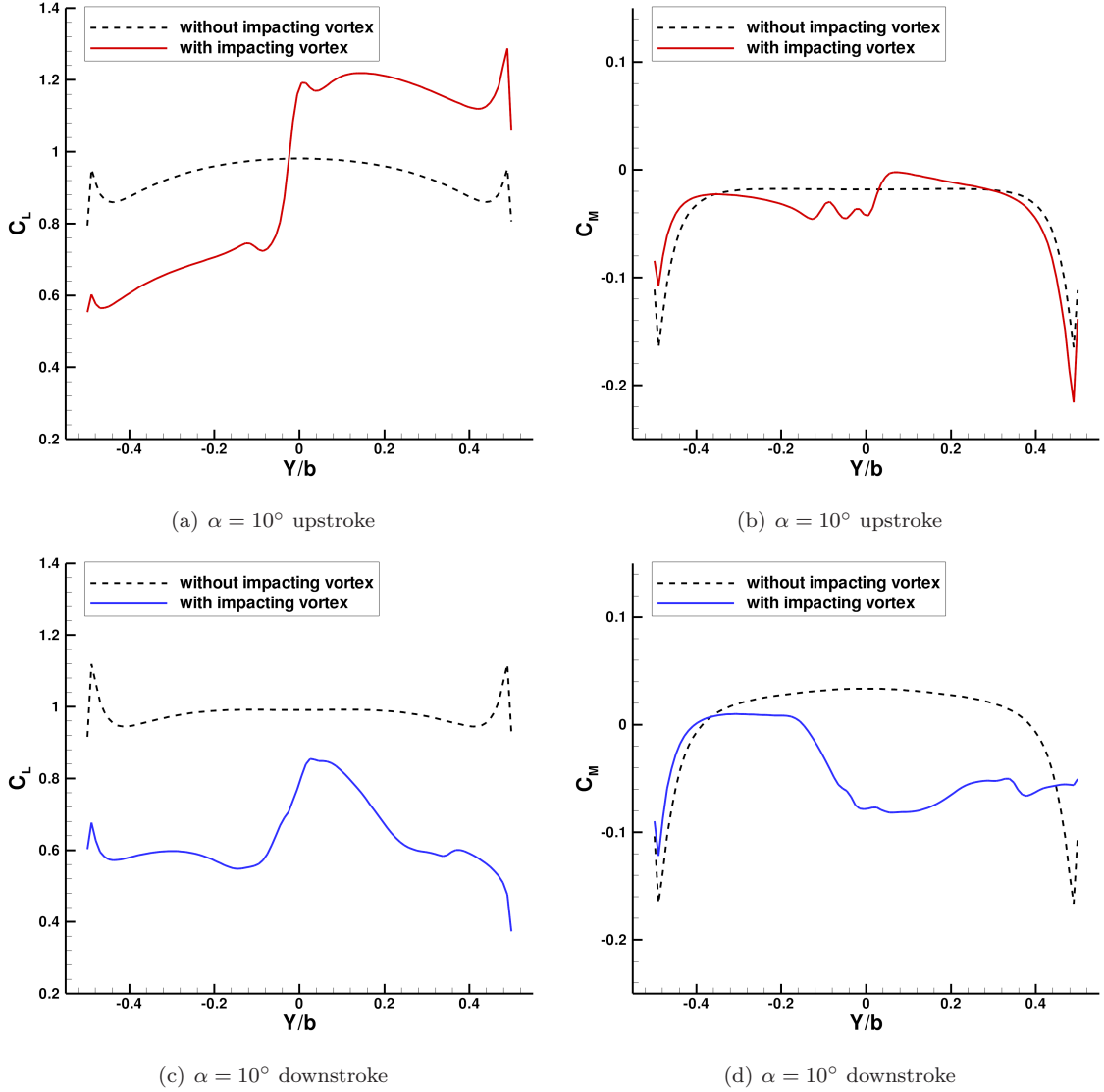
(d) $\alpha = 10°$ downstroke

Figure 20: Comparison of the airloads coefficients span-wise distribution computed by CFD with vortex interaction ($R_e = 6 \times 10^5$, $M_a = 0.09$).

the clean geometry case. Moreover, the C_P distribution on the airfoil lower surface shows a quite similar behaviour between the cases with and without the vortex interaction, with the only exception of the midspan region where a drop of the pressure peak is observed due to the vortex impact.

On the other hand, the stream-wise vortex impacting at $\alpha = 10°$ in downstroke produces an apparent decrease of the lift coefficient with respect to the clean geometry case over the entire oscillating airfoil span (see Fig. 20c). Concerning the pitching moment coefficient, an apparent drop can also be observed, in particular for positive Y (see Fig. 20d).

As mentioned earlier, the vortex impact in this phase of the motion, triggering the airfoil stall, produces

this apparent loss of performance. The stalled flow behaviour is confirmed by the C_P distribution illustrated in Fig. 21c, showing a conspicuous drop of the suction peak with respect to the clean geometry case in span-wise direction and a quite irregular chord-wise distribution. As in the previous interacting case, a drop of the pressure peak is observed on the airfoil lower surface in the region where the vortex strokes the airfoil's leading edge.

(a) $\alpha = 10°$ upstroke with impacting vortex

(b) $\alpha = 10°$ upstroke without impacting vortex

(c) $\alpha = 10°$ downstroke with impacting vortex
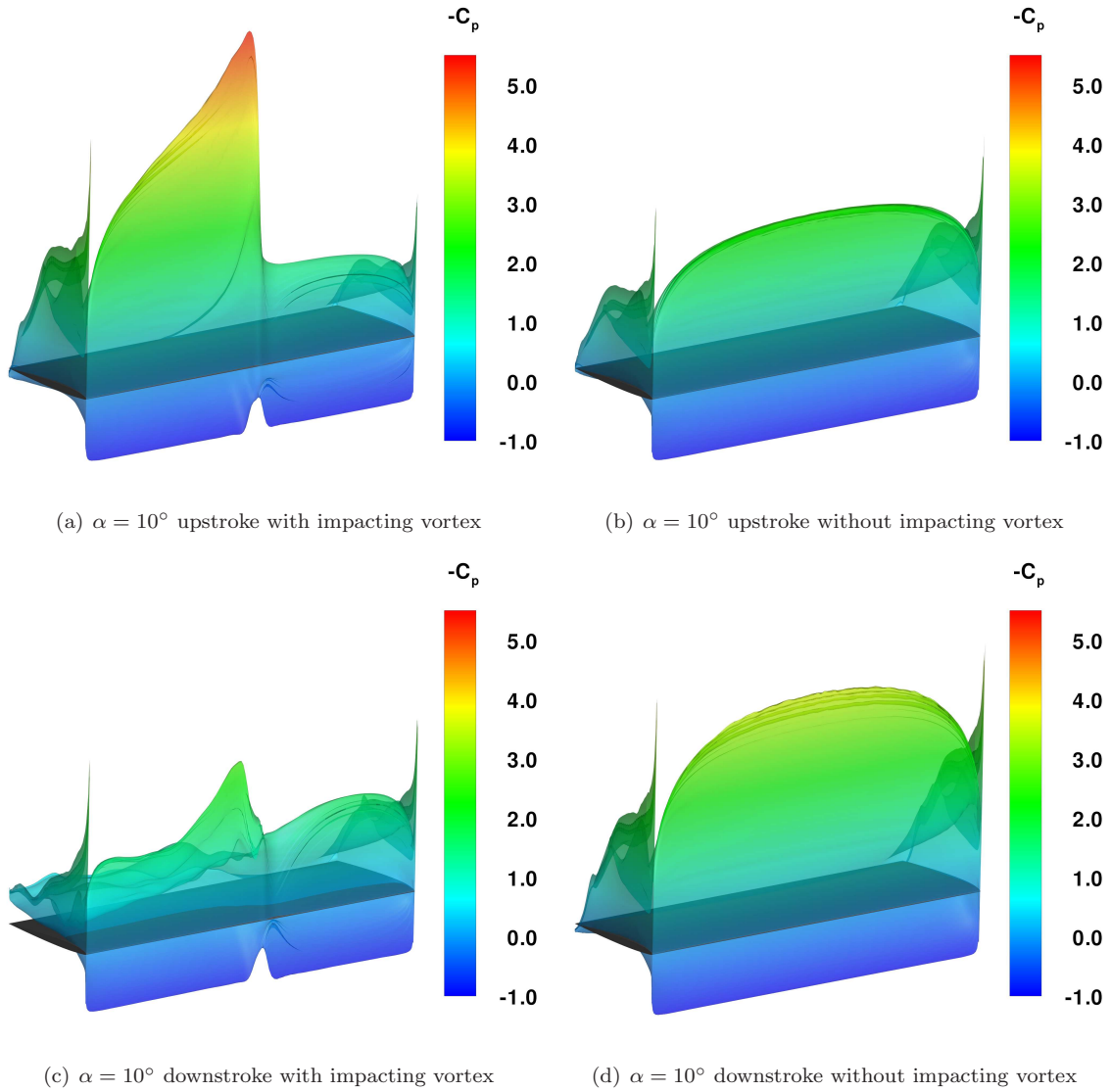
(d) $\alpha = 10°$ downstroke without impacting vortex

Figure 21: Three-dimensional distribution of the pressure coefficient C_P on the oscillating airfoil surface (($R_e = 6 \times 10^5$, $M_a = 0.09$)).

5. Conclusions

An experimental and numerical activity was carried out to investigate the effects of a perpendicular vortex interaction on the aerodynamic performance of an oscillating airfoil in light dynamic stall condition. In particular, the present work investigated the oscillating cycle with the impact of a stream-wise vortex on the leading edge of the target airfoil at the same angle of attack in upstroke and in downstroke phase of the oscillation cycle. The results of stereo PIV surveys and time-accurate simulations enabled to highlight the different effects due to the pitching motion on the interacting flow field.

In fact, significant effects are introduced on the flow around the target airfoil by the impacting vortex, depending on the phase of the interaction. While a coherent longitudinal vortex was observed on the airfoil upper surface region related to the vortex structure impinging at $\alpha = 10°$ in upstroke, the impact of the same vortex at the same angle of attack in downstroke motion produces a strong modification of the flow topology, as the interaction produces a wide back-flow region on the airfoil span-wise region where the vortex induces an upward velocity component. This different flow field behaviour, highlighted by the three-dimensional representation of the flow over the whole oscillation cycle, is due to the contributory kinematic effect induced by the rapid negative pitching rate of the airfoil, thus indicating that perpendicular vortex interactions can also introduce detrimental effects on the blade aerodynamic performance.

This important aspect was therefore investigated by the analysis of the numerical simulations results. The comparison of the lift and pitching moment cycles extracted on different span-wise sections shows that the vortex interaction for both the considered test cases produces a conspicuous increase of the aerodynamic loads hysteresis acting on the oscillating airfoil from midspan region towards the direction where the vortex induces an upward velocity component. In particular, the behaviour of the pitching moment curves extracted on this part of the airfoil span shows rapid overshoots and a severe peak representing adverse effects for the blade structure. Moreover, a net negative aerodynamic damping is observed that could lead on these sections to the risk of the stall flutter occurrence. These features, typical of the deep dynamic stall regime, shows that the vortex interaction triggers the local stall on these airfoil's sections.

A more detailed analysis was dedicated to the aerodynamic loads computed for the phases of the oscillation cycle where the stream-wise vortex impacts at the airfoil's leading edge. The span-wise distribution of the airloads compared to the one computed for the clean airfoil geometry shows that for the test case with the target airfoil at $\alpha = 10°$ in upstroke the integral lift force acting on the entire blade span is not remarkably influenced by the vortex interaction even if an apparent modification of the span-wise lift distribution is observed. On the other hand, at the same angle of attack in the downstroke an apparent loss of performance is produced by the vortex interaction, as a drop of the lift with respect to the clean geometry case is observed on the entire oscillating airfoil span.

References

Biava, M., 2007. RANS computations of rotor/fuselage unsteady interactional aerodynamics. Ph.D. thesis. Politecnico di Milano.

Biava, M., Pisoni, A., Saporiti, A., Vigevano, L., 2003. Efficient rotor aerodynamics predictions with an euler method, 29th European Rotorcraft Forum, Friedrichshafen, Germany.

Carta, F.O., 1967. An analysis of the stall flutter instability of helicopter rotor blades. Journal of the American Helicopter Society 12, 1–8.

Chan, W., Buning, P., 1995. Zipper grids for force and moment computation on overset grids, in: AIAA 1995–1681, 12th AIAA Computational Fluid Dynamics Conference, San Diego, CA, USA.

Chesshire, G., Henshaw, W.D., 1990. Composite overlapping meshes for the solution of partial differential equations. Journal of Computational Physics 90, 1–64.

Conlisk, A., 2001. Modern helicopter rotor aerodynamics. Progress in Aerospace Sciences 37, 419–476.

Costes, M., Richez, F., Le Pape, A., Gaveriaux, R., 2015. Numerical investigation of three-dimensional effects during dynamic stall. Aerospace Science and Technology 47, 216–237.

De Gregorio, F., Pengel, K., Kindler, K., 2012. A comprehensive piv measurement campaign on a fully equipped helicopter model. Experiments in Fluids 53, 37–49.

Devenport, W., Rife, M., Liapis, S., Follin, G., 1996. The structure and development of a wing-tip vortex. Journal of Fluid Mechanics 312, 67–106.

Garbaccio, S., 2011. Qualifica della Galleria del Vento del Dipartimento di Ingegneria Aerospaziale. Master's thesis. Politecnico di Milano. Milano, Italy.

Garmann, D., Visbal, M., 2015. Interactions of a streamwise-oriented vortex with a finite wing. Journal of Fluid Mechanics 767, 782–810.

Gibertini, G., Mencarelli, A., Zanotti, A., 2014. Oscillating aerofoil and perpendicular vortex interaction. Proceedings of the Institution of Mechanical Engineers, Part G: Journal of Aerospace Engineering 228, 846–858.

Glegg, S., Devenport, W., Wittmer, K., Pope, D., 1999. Broadband helicopter noise generated by blade wake interactions. Journal of the American Helicopter Society 44, 293–301.

Green, R., Coton, F., Early, J., 2006. On the three-dimensional nature of the orthogonal blade-vortex interaction. Experiments in Fluids 41, 749–761.

Green, R., Doolan, C., R, R.C., 2000. Measurements of the orthogonal blade-vortex interaction using a particle image velocimetry technique. Experiments in Fluids 29, 369–379.

Ham, N., 1975. Some conclusions from an investigation of blade-vortex interaction. Journal of the American Helicopter Society 4, 26–31.

Hirsch, C., 1988. Numerical computation of internal and external flows. John Wiley & Sons.

Horner, M., Galbraith, R., Coton, F., Stewart, J., Grant, I., 1996. Examination of vortex deformation during blade-vortex interaction. AIAA Journal 34, 1188–1194.

Hunt, J., Wray, A., Moin, P., 1988. Eddies, stream, and convergence zones in turbulent flows. Center for Turbulence Research Report CTR- S88.

Iungo, G., Skinner, P., G, G.B., 2009. Correction of wandering smoothing effects on static measurements of a wing-tip vortex. Experiments in Fluids 46, 435–452.

Jameson, A., 1991. Time dependent calculations using multigrid with applications to unsteady flows past airfoils and wings, in: AIAA 91–1596, 10th AIAA Computational Fluid Dynamics Conference, Honolulu, HI.

Kaufmann, K., Costes, M., Richez, F., Gardner, A.D., Le Pape, A., 2015. Numerical investigation of three-dimensional static and dynamic stall on a finite wing. Journal of the American Helicopter Society 60, 1–12.

Klein, A., Lutz, T., Krmer, E., Richter, K., Gardner, A.D., Altmikus, A.R.M., 2012. Numerical comparison of dynamic stall for two-dimensional airfoils and an airfoil model in the dnw-twg. Journal of the American Helicopter Society 57, 1–13.

Leishman, J.G., 1990. Dynamic stall experiments on the naca 23012 aerofoil. Experiments in Fluids 8, 49–58.

Leishman, J.G., 2000. Principles of helicopter aerodynamics. Cambridge Aerospace Series.

McCroskey, W.J., 1981. The Phenomenon of Dynamic Stall. NASA TM 81264.

PIVTEC, 2010. Pivview 2C/3C. User Manual www.pivtec.com.

Raffel, M., Willert, C., Kompenhans, J., 1998. Particle Image Velocimetry, a practical guide. Springer, Heidelberg.

Rahier, G., Delrieux, Y., 1999. Influence of vortex models on blade-vortex interaction load and noise predictions. Journal of the American Helicopter Society 44, 26–33.

Rife, M., Devenport, W., 1992. Flow Visualizations of Perpendicular Blade Vortex Interactions. NASA CR 192725.

Rockwell, D., 1998. Vortex-body interaction. Annual Review of Fluid Mechanics 30, 199–229.

Roe, P.L., 1981. Approximate riemann solvers, parameter vectors and difference schemes. Journal of Computational Physics 43, 357–372.

Schmitz, F., Yu, Y., 1983. Helicopter Impulsive Noise: Theoretical and Experimental Status. NASA TM 84390. Bell Helicopter Textron.

Shockey, G., Williamson, J., Cox, C., 1997. AH-1G Helicopter aerodynamic and structural load survey. USAAMRDL TR 76-39. Bell Helicopter Textron.

Spalart, P., Allmaras, S., 1992. One equation model for aerodynamic flows, in: AIAA 92-0439, 30th AIAA Aerospace Science Meeting & Exhibit, Reno, Nevada, USA.

Turkel, E., Radespiel, R., Kroll, N., 1997. Assessment of preconditioning methods for multidimensional aerodynamics. Computer and Fluids 26, 613–634.

Venkatakrishnan, V., 1993. On the accuracy of limiters and convergence to steady state solutions, in: AIAA 1993–880, 31st AIAA Aerospace Science Meeting & Exhibit, Reno, Nevada, USA.

Wittmer, K., Devenport, W., 1999a. Effects of perpendicular blade-vortex interaction, part 1: Turbulence structure and development. AIAA Journal 37, 805–812.

Wittmer, K., Devenport, W., 1999b. Effects of perpendicular blade-vortex interaction, part 2: Parameter study. AIAA Journal 37, 813–817.

Yu, Y., 2000. Rotor blade-vortex interaction noise. Progress in Aerospace Sciences 36, 97–115.

Zanotti, A., Auteri, F., Campanardi, G., Gibertini, G., 2011. An experimental set up for the study of the retreating blade dynamic stall, 37th European Rotorcraft Forum, Gallarate (VA), Italy.

Zanotti, A., Ermacora, M., Campanardi, G., Gibertini, G., 2014a. Stereo particle image velocimetry measurements of perpendicular blade-vortex interaction over an oscillating airfoil. Experiments in Fluids 55, 1–13.

Zanotti, A., Gibertini, G., 2013. Experimental investigation of the dynamic stall phenomenon on a naca 23012 oscillating aerofoil. Proceedings of the Institution of Mechanical Engineers, Part G: Journal of Aerospace Engineering 227, 1375–1388.

Zanotti, A., Nilifard, R., Gibertini, G., Guardone, A., Quaranta, G., 2014b. Assessment of 2d/3d numerical modeling for deep dynamic stall experiments. Journal of Fluids and Structures 51, 97–115.

Zioutis, X.K., Spyropoulos, A.I., Margaris, D.P., Papanikas, D.G., 2004. Numerical investigation of bvi modeling effects on helicopter rotor free wake, 24th International Congress of the Aeronautical Sciences, Yokohama, Japan.